POLITECNICO
MILANO 1863

SCUOLA DI INGEGNERIA INDUSTRIALE
E DELL'INFORMAZIONE

Executive Summary of the Thesis

Dynamic Analysis of Tiltrotor Drive Train configurations

Laurea Magistrale in Aeronautical Engineering - Ingegneria Aeronautica

Author: Manikanda Krishnan Janarthanan

Advisor: Prof. Masarati Pierangelo

Co-advisor:

Academic year: 2025-2026

Abstract

Tiltrotor aircraft combine vertical takeoff capability with efficient fixed-wing cruise, but their mechanically interconnected propulsion systems introduce substantial drivetrain complexity and dynamic coupling. Recent drivetrain-related incidents have emphasized the importance of understanding load redistribution and interaction mechanisms within coupled rotor–drivetrain systems. In particular, the influence of proprotor blade dynamics on drivetrain behavior remains insufficiently characterized. This study develops two complementary modeling approaches for integrated tiltrotor dynamic analysis. First, a finite element model is established to rigorously derive the governing equations describing how the collective lead–lag motion of rotor blades influences drivetrain torsional dynamics through inertial and elastic coupling. The formulation explicitly captures the additional dynamic loads induced by synchronized blade lead–lag motion and their effect on shaft torque and gearbox response. Second, a sensitivity analysis is formulated for a linear time-invariant (LTI) model to establish a unified analytical framework for evaluating the stability of the tiltrotor drivetrain with respect to variations in key drivetrain components. The primary elements considered include the planetary gears, central gear, engine gear, engine, and their corresponding output shafts. Results demonstrate the capability of the proposed framework to capture rotor–drivetrain interaction mechanisms, providing insight for reliability assessment, fault diagnosis, and future drivetrain design improvement.

Keywords: Gear systems, Rotorcraft dynamics, Multiblade coordinates, Collective lead-lag hub-torsional coupling, Eigen Sensitivity

1. Introduction

Tiltrotor aircraft combine the vertical takeoff and landing capability of helicopters with the cruise efficiency of fixed-wing airplanes. The Bell Boeing V-22 Osprey represents one of the most advanced implementations of this configuration. However, the mechanical complexity of its drivetrain system has raised persistent safety concerns.

In November 2023, a fatal crash involving a V-22 led to the temporary grounding of the fleet. According to official information released by the U.S. Navy, the accident was attributed to the failure of a propulsion system component within the proprotor gearbox assembly. The drivetrain of the aircraft includes critical elements such as the input quill assembly and the sprag clutch,

which ensure torque transmission and synchronized rotor speed. The reported failure occurred in a manner described as unprecedented, prompting renewed scrutiny of propulsion system reliability and the implementation of additional safety measures before flight operations resumed (U.S. Navy, 2024 [1]).
This event is not isolated. Previous accidents involving the V-22 Osprey have also been associated with drivetrain-related issues. For example, investigations into earlier mishaps identified failures within gearbox components and clutch mechanisms that affected torque transfer and rotor synchronization. These incidents demonstrate the sensitivity of tiltrotor aircraft to drivetrain integrity, where component malfunction can rapidly compromise aircraft stability and controllability.
The recurrence of drivetrain-related failures in tiltrotor operations highlights a critical need for improved modeling, fault prediction, and structural reliability assessment of power transmission systems. Despite advances in aerospace drivetrain design, existing analytical and simulation approaches may not fully capture complex load interactions, transient behavior, and failure progression under operational conditions. Therefore, a systematic modeling strategy is required to better understand and mitigate the risks associated with critical propulsion components in tiltrotor aircraft.

2. Modeling Strategy

In this work, finite element modeling (FEM) is carried out for the gear system and the rotor assembly. The gear model captures the structural and dynamic characteristics of the transmission elements, while the rotor model represents the primary load and dynamic response of the rotating system. Together, these models provide a basis for analyzing the mechanical behavior of the Tilt rotor drive train.

2.1. Geared System

A typical geared chain system consisting of a single simple gear used to regulate the rotational speeds of two mounted shafts is illustrated in Figure 1a. A simplified mathematical representation of a single gear pair in Figure 1b is adopted, which can be applied to various gear types, including spur, bevel, and screw gears.

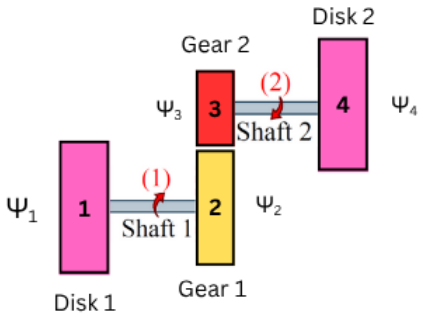

(a) A typical gear chain system

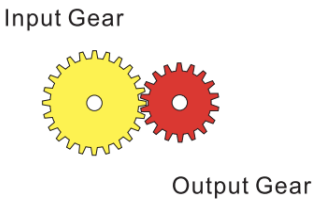

(b) SimpleGear.

Figure 1: Geared Chain System

In this study, the gears are treated as kinematically and dynamically ideal components. Tooth compliance is neglected, and effects such as non-smooth contact dynamics, variations in the number of teeth simultaneously in contact, as well as associated phenomena like rattling and torque ripple, are not considered. Additionally, power losses resulting from friction or other dissipative effects are excluded from the analysis. Under the assumptions of concentrated (lumped) masses and a massless, flexible shaft, the geared system is represented as a purely one-dimensional mechanical model. This simplified configuration forms the foundation of the analytical framework developed in this work.
The free torsional vibration equation of the elastic shaft and rigid disk is

$$\boldsymbol{M}\ddot{\boldsymbol{X}} + \boldsymbol{K}\boldsymbol{X} = 0 \tag{1a}$$

Input gear,

$$\begin{bmatrix} J_1 & 0 \\ 0 & J_2 \end{bmatrix} \begin{bmatrix} \ddot{\psi}_1 \\ \ddot{\psi}_2 \end{bmatrix} + K_1 \begin{bmatrix} 1 & -1 \\ -1 & 1 \end{bmatrix} \begin{bmatrix} \psi_1 \\ \psi_2 \end{bmatrix} = 0 \tag{1b}$$

Output gear,

$$\begin{bmatrix} J_3 & 0 \\ 0 & J_4 \end{bmatrix} \begin{bmatrix} \ddot{\psi}_3 \\ \ddot{\psi}_4 \end{bmatrix} + K_2 \begin{bmatrix} 1 & -1 \\ -1 & 1 \end{bmatrix} \begin{bmatrix} \psi_3 \\ \psi_4 \end{bmatrix} = 0 \tag{1c}$$

where $J_{1,2,3,4}$ are the associated moment of Inertia of the Disks 1,2,3 & 4. $K_{1,2}$ are the torsional stiffness of the shaft 1 & 2 and $\psi_{1,2,3,4}$ are the associated angular displacement of the Disk 1,2,3 & 4.
The Constriant Equation,

$$\phi = N_3\psi_3 - N_2\psi_2 = 0 \tag{2}$$

Gear Ratio n is defined as,

$$n = \frac{\psi_3}{\psi_2} = \frac{N_2}{N_3} \tag{3}$$

where N_2&N_3 are number of teeth in gear 2 and 3.
The resulting DAEs that describe the constrained dynamics problem can be solved directly considering the Lagrange multipliers as additional unknowns, resulting in the socalled redundant coordinate set (RCS) formulation 2.1.2 or by using miminal coordinate set approach 2.1.1, the problem can be manipulated and transformed into the corresponding underlying ODE problem, reducing the set of coordinates to the truly independent (Lagrangian) ones Ref. [8].

2.1.1 Minimal Coordinate Set

$$\boldsymbol{X} = \begin{bmatrix}\psi_1\\ \psi_2\\ \psi_3\\ \psi_4\end{bmatrix} = \begin{bmatrix}1 & 0 & 0\\ 0 & 1 & 0\\ 0 & n & 0\\ 0 & 0 & 1\end{bmatrix}\begin{bmatrix}\psi_1\\ \psi_2\\ \psi_4\end{bmatrix} = \boldsymbol{T\psi} \tag{4}$$

here T is the projection matrix.

$$\boldsymbol{MT\ddot{\psi} + KT\psi} = 0 \tag{5}$$

$$\boldsymbol{T^T(MT\ddot{\psi} + KT\psi)} = 0 \tag{6}$$

$$\hat{\boldsymbol{M}}\ddot{\boldsymbol{\psi}} + \hat{\boldsymbol{K}}\boldsymbol{\psi} = 0 \tag{7a}$$

$$\hat{\boldsymbol{M}} = \boldsymbol{T^T MT} \tag{7b}$$

$$\hat{\boldsymbol{K}} = \boldsymbol{T^T KT} \tag{7c}$$

The reduced order Inertia and Stiffness matrix are as follows,

$$\hat{\boldsymbol{M}} = \begin{bmatrix}J_1 & 0 & 0\\ 0 & J_2 + n^2J_3 & 0\\ 0 & 0 & J_4\end{bmatrix} \tag{7d}$$

$$\hat{\boldsymbol{K}} = \begin{bmatrix}K_1 & -K_1 & 0\\ -K_1 & K_1 + n^2K_2 & -nK_2\\ 0 & -nK_2 & K_2\end{bmatrix} \tag{7e}$$

In this formulation, $J_2 + n^2J_3$ denote the equivalent inertia of the gear assembly, transformed through the gear ratio n. A comprehensive discussion is provided in the section 3.1.1 addressing tiltrotor drivetrain configurations.

2.1.2 Redundant Co-ordinate set

The jacobian of the equation (2) with respect to $(\psi_1, \psi_2, \psi_3, \psi_4)$ yields the constraint Jacobian matrix,

$$\boldsymbol{\phi_{/X}} = \begin{bmatrix}0 & -N_2 & N_3 & 0\end{bmatrix} \tag{8}$$

This matrix characterizes the linearized relationship between the constraint and the system coordinates and plays a central role in enforcing the kinematic constraint within the redundant coordinate framework.

$$\boldsymbol{M\ddot{X} + KX + \phi_{/X}^T\lambda} = 0 \tag{9a}$$

$$\boldsymbol{\phi_{/X}X} = 0 \tag{9b}$$

$$\begin{bmatrix}\boldsymbol{M} & 0\\ 0 & 0\end{bmatrix}\begin{bmatrix}\ddot{\boldsymbol{X}}\\ \ddot{\lambda}\end{bmatrix} + \begin{bmatrix}\boldsymbol{K} & \boldsymbol{\phi_{/X}^T}\\ \boldsymbol{\phi_{/X}} & 0\end{bmatrix}\begin{bmatrix}\boldsymbol{X}\\ \lambda\end{bmatrix} = 0 \tag{9c}$$

The resulting system consists of the dynamic equilibrium equation and the algebraic constraint equation, forming a coupled set of differential–algebraic equations. In matrix form, the augmented system clearly shows the interaction between the physical coordinates and the Lagrange multiplier, ensuring that the constraint is satisfied at all times during the motion.

2.2. Sensitivity of Stability Properties for LTI Systems

This study is to evaluate the analytical sensitivity for rotor blade and drive train variables. Here the sensitivity of a Linear Time Invariant (LTI) system is analysed, details in Ref. [9].
Consider a LTI system,

$$\boldsymbol{x' = Ax} \tag{10}$$

Its eigensolution is thus the solution of

$$(s\boldsymbol{I} - \boldsymbol{A})\boldsymbol{X} = 0 \tag{11}$$

Once the eigensolution is found, its sensitivity can be studied by considering the partial derivative of the eigenproblem with respect to a generic parameter p, which gives,

$$s_{/p}\boldsymbol{x} - \boldsymbol{A_{/p}x} + (s\boldsymbol{I} - \boldsymbol{A})\boldsymbol{x_{/p}} = 0 \tag{12}$$

The number of degrees of freedom in Eq. 10 is u. Eq. 12 provides u equations whereas there are $u+1$ unknowns since both of $s_{/p}$ (1 unknown) and $\boldsymbol{x_{/p}}$ (n unknowns) are needed to be evaluated. One more equation is required and it comes from augmenting the problem with the eigenvector being normalized with the L^∞ norm of X,

$$\boldsymbol{g^T x} = 1 \tag{13}$$

where g is a real valued vector whose elements are zero everywhere and unity for the index of eigen vector with largest magnitude. This method is adopted from an under review Paper Ref. [6].
which yield,

$$s_{/p}\boldsymbol{x} - \boldsymbol{A_{/p}x} + (s\boldsymbol{I} - \boldsymbol{A})\boldsymbol{x_{/p}} = 0 \tag{14a}$$

$$\boldsymbol{g^T x_{/p}} = 0 \tag{14b}$$

$$\begin{bmatrix} (s\boldsymbol{I} - \boldsymbol{A}) & \boldsymbol{x} \\ \boldsymbol{g^T} & 0 \end{bmatrix} \begin{bmatrix} \boldsymbol{x_{/p}} \\ s_{/p} \end{bmatrix} = \begin{bmatrix} \boldsymbol{A_{/p}x} \\ 0 \end{bmatrix} \tag{14c}$$

Now, sensitivity of a system can be studied by only changing the rhs of Eq. 14.

2.3. Rotating Blade

2.3.1 Rigid Blade Lag Kinematics

Consider a rotor, rotating at a constant angular velocity Ω with respect to the airframe. The rotor blades (rigid) are only allowed free lagging (leag-lag motion ξ) about a lead-lag hinge that is offset by e_r from the hub center (axis of rotation). In a reference frame that is rotating with the hub, the blade is subjected to a centrifugal force which depends on the distance r from hinge point, but remains in-plane.

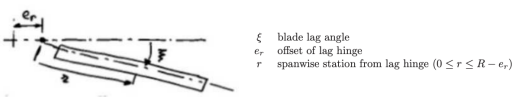

Figure 2: Lead-Lag

Considering the lag (or lead-lag) motion alone, The position of a generic point P on the blade, in the hub reference system, is

$$\boldsymbol{p} = \begin{bmatrix} e_r + r\cos\xi \\ -r\sin\xi \\ 0 \end{bmatrix} \tag{15}$$

The Virtual displacement associated with the generalized coordinate ξ is

$$\boldsymbol{\delta p} = \begin{bmatrix} -r\sin\xi \\ -r\cos\xi \\ 0 \end{bmatrix} \delta\xi \tag{16}$$

Differentiating Eq 15 gives the relative velocity due to lag motion:

$$\dot{\boldsymbol{p}} = \begin{bmatrix} -r\sin\xi \\ -r\cos\xi \\ 0 \end{bmatrix} \dot{\xi} \tag{17}$$

Differentiating Eq 17 gives relative acceleration:

$$\ddot{\boldsymbol{p}} = -\begin{bmatrix} r\sin\xi \\ r\cos\xi \\ 0 \end{bmatrix} \ddot{\xi} + \begin{bmatrix} -r\cos\xi \\ r\sin\xi \\ 0 \end{bmatrix} \dot{\xi}^2 \tag{18}$$

The first term represents tangential acceleration, while the second corresponds to centripetal acceleration.

2.3.2 Kinematics in Non-Rotating Frame with mast motion

The motion of the hub eventually induces motion on the blade and modifies inertial matrices. The position of a point on a blade in non-rotating reference frame $\boldsymbol{Q}$ is a function of the hub the orientation of the blade with respect to non-rotating frame $\boldsymbol{R}$ times the position of that point on the blade $\boldsymbol{p}$ in rotating frame.
Position in non-rotating frame:

$$\boldsymbol{Q} = \boldsymbol{Rp} \tag{19}$$

where $\boldsymbol{R(\psi)}$ is the transformation matrix from rotating to non-rotating reference frame.

$$\boldsymbol{R} = \begin{bmatrix} \cos\psi & -\sin\psi & 0 \\ \sin\psi & \cos\psi & 0 \\ 0 & 0 & 1 \end{bmatrix} \tag{20}$$

Virtual displacement:

$$\boldsymbol{\delta Q} = \boldsymbol{R\delta p} + \boldsymbol{\psi_\delta} \times \boldsymbol{Rp} \tag{21}$$

where $\boldsymbol{\psi_\delta}$ is the perturbation of hub orientation.

Differentiating Eq 19 gives velocity in non rotating frame.
Velocity:

$$\dot{\boldsymbol{Q}} = \boldsymbol{\Omega} \times \boldsymbol{Rp} + \boldsymbol{R\dot{p}} \tag{22}$$

where,

$$\boldsymbol{\Omega}\times = \begin{bmatrix} 0 & -\Omega & 0 \\ \Omega & 0 & 0 \\ 0 & 0 & 0 \end{bmatrix}$$

$$\dot{\boldsymbol{R}} = \boldsymbol{\Omega} \times \boldsymbol{R}$$

Differentiating Eq 22 gives acceleration in non rotating frame.
Acceleration:

$$\ddot{\boldsymbol{Q}} = \dot{\boldsymbol{\Omega}} \times \boldsymbol{Rp} + \boldsymbol{R\ddot{p}} + 2\boldsymbol{\Omega} \times \boldsymbol{R\dot{p}} + \boldsymbol{\Omega} \times \boldsymbol{\Omega} \times \boldsymbol{Rp} \tag{24}$$

The load in non-rotating reference frame can be expressed as

$$\boldsymbol{F_{in}} = -m\ddot{\boldsymbol{Q}} \tag{25a}$$

$$\boldsymbol{F_{in}} = -m(\dot{\boldsymbol{\Omega}} \times \boldsymbol{Rp} + \boldsymbol{R\ddot{p}} + 2\boldsymbol{\Omega} \times \boldsymbol{R\dot{p}} + \boldsymbol{\Omega} \times \boldsymbol{\Omega} \times \boldsymbol{Rp}) \tag{25b}$$

2.3.3 Virtual Work of Inertia Forces

The virtual work of the forces acting on the entire blade is

$$\delta \boldsymbol{W}_{ine} = -\int_0^{R-e_r} \delta \boldsymbol{Q}^T \, \boldsymbol{F_{in}} dr \tag{26a}$$

$$\delta \boldsymbol{W}_{ine} = -\int_0^{R-e_r} \delta \boldsymbol{Q}^T \, m\ddot{\boldsymbol{Q}} \, dr \tag{26b}$$

$$\begin{aligned} \delta \boldsymbol{W}_{ine} = & -\int \delta\xi^T m \left(er\Omega^2 \sin\xi \right. \\ & \left. -r\dot{\Omega}(r + e_r \cos\xi) + r^2\ddot{\xi} \right) dr \\ & -\int \delta\psi^T m \left((e_r^2 + 2er\cos\xi + r^2)\dot{\Omega} \right. \\ & + r(r\ddot{\xi} - e_r \sin\xi \, \dot{\xi}^2 + e_r \cos\xi \, \ddot{\xi}) \\ & \left. -2er \sin\xi \, \Omega\dot{\xi} \right) dr \end{aligned} \tag{27}$$

Linearization about the steady uniform rotational motion

The system variables are decomposed into a steady-state rotational component and small perturbations about this reference motion. Here, Ω_0 represents the constant nominal angular velocity, and $\Delta\psi$, $\Delta\Omega$, $\Delta\xi$ denote small dynamic deviations from the steady operating condition.

$$\Omega = \Omega_0 + \Delta\Omega = \Omega_0 + \Delta\dot{\psi} \quad (\Omega_0 = constant) \tag{28a}$$

$$\psi = \Omega_0 t + \Delta\psi \tag{28b}$$

$$\dot{\Omega} = \dot{\Omega}_0 + \Delta\dot{\Omega} = \Delta\dot{\Omega} = \Delta\ddot{\psi} \quad (\dot{\Omega}_0 = 0) \tag{28c}$$

$$\xi = \bar{\xi} + \Delta\xi = \Delta\xi \quad (\bar{\xi} = 0) \tag{28d}$$

The steady conditions $\bar{x}$ is as follows,

$$(\ddot{\bar{\xi}}, \dot{\bar{\xi}}, \bar{\xi}) = (0, 0, 0)$$

$$(\ddot{\psi}_0, \dot{\psi}_0, \psi_0) = (0, \Omega_0, \Omega_0 t)$$

The nonlinear system in Equation 27 was linearized about the steady conditions.

$$\begin{aligned} \delta \boldsymbol{W}_{ine} = & \\ & -\begin{bmatrix} \delta\xi \\ \delta\psi \end{bmatrix}^T \left(\int_0^{R-e_r} m \begin{bmatrix} r^2 & -r(e_r + r) \\ -r(e_r + r) & (e_r + r)^2 \end{bmatrix} \begin{bmatrix} \ddot{\xi} \\ \ddot{\psi} \end{bmatrix} dr \right. \\ & \left. + \begin{bmatrix} e_r\Omega_0^2 r & 0 \\ 0 & 0 \end{bmatrix} \begin{bmatrix} \xi \\ \psi \end{bmatrix} \right) = 0 \end{aligned} \tag{29}$$

taking $\Delta\xi = \xi$ and $\Delta\psi = \psi$

$$\begin{aligned} \delta \boldsymbol{W}_{ine} = & \\ & -\int_0^{R-e_r} \begin{bmatrix} \delta\xi \\ \delta\psi \end{bmatrix}^T m \left(\begin{bmatrix} r^2 & -r(e_r + r) \\ -r(e_r + r) & (e_r + r)^2 \end{bmatrix} \begin{bmatrix} \ddot{\xi} \\ \ddot{\psi} \end{bmatrix} \right. \\ & \left. + \begin{bmatrix} e_r\Omega_0^2 r & 0 \\ 0 & 0 \end{bmatrix} \begin{bmatrix} \xi \\ \psi \end{bmatrix} \right) dr \end{aligned} \tag{30}$$

The Eq. 30 describes the dynamics of lead-lag motion of one blade attached with the hub and explicitly captures the inertial coupling between the lead–lag motion and the rotor azimuth ψ.

2.3.4 Dynamics of Multi-Blade, with Hub Motion

Introducing the first- and second-order moment of inertia,

$$\int_0^{R-e_r} mr^2 dr = J_{\xi\xi} \tag{31}$$

$$\int_0^{R-e_r} mr(e_r + r)dr = J_{\xi\psi} = J_{\psi\xi} \tag{32}$$

$$\int_0^{R-e_r} m(e_r + r)^2 dr = J_{\psi\psi} \tag{33}$$

$$\int_0^{R-e_r} mrdr = S_{\xi} \tag{34}$$

$$\delta \boldsymbol{W}_{ine} = -\begin{bmatrix}\delta\xi \\ \delta\psi\end{bmatrix}^T \left(\begin{bmatrix} J_{\xi\xi} & -J_{\xi\psi} \\ -J_{\psi\xi} & J_{\psi\psi}\end{bmatrix} \begin{bmatrix}\ddot{\xi} \\ \ddot{\psi}\end{bmatrix} + \begin{bmatrix} e_r\Omega_0^2 S_\xi & 0 \\ 0 & 0\end{bmatrix} \begin{bmatrix}\xi \\ \psi\end{bmatrix} \right) = 0 \tag{35}$$

The lead-lag rotations of all blades, N_b is the number of blades. Each blade is modeled with their corresponding lead-lag and hub coupling, forming a block-diagonal matrix.

$$\begin{bmatrix} J_{\xi\xi} & -J_{\xi\psi} & \cdots & 0 & 0 \\ -J_{\psi\xi} & J_{\psi\psi} & \cdots & 0 & 0 \\ \vdots & \vdots & \ddots & \vdots & \vdots \\ 0 & 0 & \cdots & J_{\xi\xi} & -J_{\xi\psi} \\ 0 & 0 & \cdots & -J_{\psi\xi} & J_{\psi\psi} \end{bmatrix} \begin{bmatrix} \ddot{\xi}_1 \\ \ddot{\psi}_1 \\ \vdots \\ \ddot{\xi}_{N_b} \\ \ddot{\psi}_{N_b} \end{bmatrix} - \begin{bmatrix} e_r\Omega_0^2 S_\xi & 0 & \cdots & 0 & 0 \\ 0 & 0 & \cdots & 0 & 0 \\ \vdots & \vdots & \ddots & \vdots & \vdots \\ 0 & 0 & \cdots & e_r\Omega_0^2 S_\xi & 0 \\ 0 & 0 & \cdots & 0 & 0 \end{bmatrix} \begin{bmatrix} \xi_1 \\ \psi_1 \\ \vdots \\ \xi_{N_b} \\ \psi_{N_b} \end{bmatrix} = 0 \tag{36}$$

Since hub perturbation for all the blades are same which gives, $\psi_1 = \psi_2 = \cdots = \psi_{N_b}$
The constraint equation is given by,

$$\boldsymbol{\phi} = \begin{bmatrix} \psi_1 - \psi_{N_b} \\ \psi_2 - \psi_{N_b} \\ \vdots \\ \psi_{N_b-1} - \psi_{N_b} \end{bmatrix} = 0 \tag{37}$$

Using the minimal coordinate set approach, the constraint 37 is incorporated into Eq. 36, which reduces the system to its independent degrees of freedom while inherently satisfying the kinematic constraints.

$$\begin{bmatrix} \xi_1 \\ \psi_1 \\ \xi_2 \\ \psi_2 \\ \vdots \\ \xi_{N_b} \\ \psi_{N_b} \end{bmatrix} = \begin{bmatrix} 1 & 0 & 0 & \cdots & 0 & 0 \\ 0 & 0 & 0 & \cdots & 0 & 1 \\ 0 & 1 & 0 & \cdots & 0 & 0 \\ 0 & 0 & 0 & \cdots & 0 & 1 \\ \vdots & \vdots & \vdots & \ddots & \vdots & \vdots \\ 0 & 0 & 0 & \cdots & 1 & 0 \\ 0 & 0 & 0 & \cdots & 0 & 1 \end{bmatrix} \begin{bmatrix} \xi_1 \\ \xi_2 \\ \vdots \\ \xi_{N_b} \\ \psi_{N_b} \end{bmatrix} = \boldsymbol{T}\boldsymbol{q} \tag{38}$$

where $\boldsymbol{T}$ is the transformation matrix and $\dot{\boldsymbol{T}} = 0$.

$$-\boldsymbol{T}' \begin{bmatrix} J_{\xi\xi} & -J_{\xi\psi} & \cdots & 0 & 0 \\ -J_{\psi\xi} & J_{\psi\psi} & \cdots & 0 & 0 \\ \vdots & \vdots & \ddots & \vdots & \vdots \\ 0 & 0 & \cdots & J_{\xi\xi} & -J_{\xi\psi} \\ 0 & 0 & \cdots & -J_{\psi\xi} & J_{\psi\psi} \end{bmatrix} \boldsymbol{T}\ddot{\boldsymbol{q}}$$
$$-\boldsymbol{T}' \begin{bmatrix} e_r\Omega_0^2 S_\xi & 0 & \cdots & 0 & 0 \\ 0 & 0 & \cdots & 0 & 0 \\ \vdots & \vdots & \ddots & \vdots & \vdots \\ 0 & 0 & \cdots & e_r\Omega_0^2 S_\xi & 0 \\ 0 & 0 & \cdots & 0 & 0 \end{bmatrix} \boldsymbol{T}\boldsymbol{q} = 0 \tag{39}$$

For our current purposes, we can approximate hingeless rotor designs using an equivalent articulated design with an additional root lag spring of stiffness k_ξ and damper c_ξ, whose contribution to the generalized forces, according to Lagrange's formalism, is

$$f_{\xi_i} = -k_\xi\, \xi_i - c_\xi\, \dot{\xi}_i \tag{40}$$

ξ_i corresponds to the lag motion of i-th blade.

The resulting equation of motion is

$$\begin{bmatrix} J_{\xi\xi} & \cdots & 0 & -J_{\xi\psi} \\ \vdots & \ddots & \vdots & \vdots \\ 0 & \cdots & J_{\xi\xi} & -J_{\xi\psi} \\ -J_{\psi\xi} & \cdots & -J_{\psi\xi} & N_b J_{\psi\psi} \end{bmatrix} \begin{bmatrix} \ddot{\xi}_1 \\ \vdots \\ \ddot{\xi}_{N_b} \\ \ddot{\psi} \end{bmatrix} + \begin{bmatrix} c_\xi & \cdots & 0 & 0 \\ \vdots & \ddots & \vdots & \vdots \\ 0 & \cdots & c_\xi & 0 \\ 0 & \cdots & 0 & 0 \end{bmatrix} \begin{bmatrix} \dot{\xi}_1 \\ \vdots \\ \dot{\xi}_{N_b} \\ \dot{\psi} \end{bmatrix}$$
$$+ \begin{bmatrix} e_r\Omega_0^2 S_\xi + k_\xi & \cdots & 0 & 0 \\ \vdots & \ddots & \vdots & \vdots \\ 0 & \cdots & e_r\Omega_0^2 S_\xi + k_\xi & 0 \\ 0 & \cdots & 0 & 0 \end{bmatrix} \begin{bmatrix} \xi_1 \\ \vdots \\ \xi_{N_b} \\ \psi \end{bmatrix} = 0 \tag{41a}$$

representing in a symbolic form gives,

$$\hat{\boldsymbol{M}}_{\boldsymbol{b}}\ddot{\hat{\boldsymbol{q}}}_{\boldsymbol{b}} + \hat{\boldsymbol{C}}_{\boldsymbol{b}}\dot{\hat{\boldsymbol{q}}}_{\boldsymbol{b}} + \hat{\boldsymbol{K}}_{\boldsymbol{b}}\hat{\boldsymbol{q}}_{\boldsymbol{b}} = 0 \tag{41b}$$

Note that the blade inertia submatrix is diagonal; however, the coupling terms between the blade lead–lag coordinates and the hub coordinate introduce non-zero off-diagonal entries, rendering the full inertia matrix non-diagonal because of the constraint 37.

2.3.5 Multiblade Coordinates

In order to analyze rotorcraft all together with its rotating and non-rotating components, the perturbation matrices in rotating reference frame should be transformed to an inertial reference frame. For this reason, the multiblade coordinate transformation is being used.
The coordinate transformation taken from Ref. [9]

$$\xi_m = \xi_0 + \sum_{n=1}^{N_c} \Big[\cos(n\psi_m)\, \xi_{nc} + \sin(n\psi_m)\, \xi_{ns} \Big] + (-1)^m \xi_{N_b/2} \tag{42}$$

where, N_b is the number of blades, ξ_0 is the collective lead-lag motion and ξ_{nc} & ξ_{ns} are the cyclic lead-lag motions all of which are in non-rotating frame , ψ_m is the azimuth of blade. $\xi_{N_b/2}$ of the multiblade coordinates vector, are only present when N_b is even. The multiblade coordinates are applicable to rotors with $N_b > 3$.

$$\begin{bmatrix} \xi_1 \\ \xi_2 \\ \vdots \\ \xi_{N_b} \\ \psi \end{bmatrix} = \begin{bmatrix} 1 & \cos\psi_1 & \sin\psi_1 & \cos(2\psi_1) & \sin(2\psi_1) & \dots & (-1)^1 & 0 \\ 1 & \cos\psi_2 & \sin\psi_2 & \cos(2\psi_2) & \sin(2\psi_2) & \dots & (-1)^2 & 0 \\ \vdots & \vdots & \vdots & \vdots & \vdots & \ddots & \vdots & 0 \\ 1 & \cos\psi_{N_b} & \sin\psi_{N_b} & \cos(2\psi_{N_b}) & \sin(2\psi_{N_b}) & \dots & (-1)^{N_b} & 0 \\ 0 & 0 & 0 & 0 & 0 & \cdots & 0 & 1 \end{bmatrix} \begin{bmatrix} \xi_0 \\ \xi_{1c} \\ \xi_{1s} \\ \xi_{2c} \\ \xi_{2s} \\ \vdots \\ \xi_{N_b/2} \\ \psi \end{bmatrix} \tag{43}$$

the Eq. 43 is written in form $\hat{\boldsymbol{q}}_{\boldsymbol{b}} = \mathbf{H}\boldsymbol{q}_{\boldsymbol{b}}$, $\mathbf{H}$ is the multiblade-transformation matrix.
Differentiating Eq. 43 once and twice yields,

$$\dot{\hat{\boldsymbol{q}}}_{\boldsymbol{b}} = \dot{\mathbf{H}}\boldsymbol{q}_{\boldsymbol{b}} + \mathbf{H}\dot{\boldsymbol{q}}_{\boldsymbol{b}} \tag{44}$$

$$\ddot{\hat{\boldsymbol{q}}}_{\boldsymbol{b}} = \ddot{\mathbf{H}}\boldsymbol{q}_{\boldsymbol{b}} + 2\dot{\mathbf{H}}\dot{\boldsymbol{q}}_{\boldsymbol{b}} + \mathbf{H}\ddot{\boldsymbol{q}}_{\boldsymbol{b}} \tag{45}$$

Modeling Eq. 41 in Mutliblade Coordinates yields,

$$\boldsymbol{M_b}\, \ddot{\boldsymbol{q}}_{\boldsymbol{b}} + \boldsymbol{C_b}\, \dot{\boldsymbol{q}}_{\boldsymbol{b}} + \boldsymbol{K_b}\, \boldsymbol{q}_{\boldsymbol{b}} = 0$$

where,

$$\boldsymbol{M_b} = \boldsymbol{H}^T \hat{\boldsymbol{M}}_{\boldsymbol{b}} \boldsymbol{H} \tag{46a}$$

$$\boldsymbol{C_b} = \boldsymbol{H}^T (\hat{\boldsymbol{C}}_{\boldsymbol{b}} \boldsymbol{H} + 2\hat{\boldsymbol{M}}_{\boldsymbol{b}} \dot{\boldsymbol{H}}) \tag{46b}$$

$$\boldsymbol{K_b} = \boldsymbol{H}^T (\hat{\boldsymbol{K}}_{\boldsymbol{b}} \boldsymbol{H} + \hat{\boldsymbol{C}}_{\boldsymbol{b}} \dot{\boldsymbol{H}} + \hat{\boldsymbol{M}}_{\boldsymbol{b}} \ddot{\boldsymbol{H}}) \tag{46c}$$

(46d)

If we consider only the 1st-order harmonics, $\ddot{\boldsymbol{H}}$ and $\dot{\boldsymbol{H}}$ has no coupling effects with ψ.

The first block, consisting of two equations, the collective lead-lag motion ξ_0 coupled with Hub rotation ψ,

$$N_b \left(\begin{bmatrix} J_{\xi\xi} & -J_{\xi\psi} \\ -J_{\psi\xi} & J_{\psi\psi} \end{bmatrix} \begin{bmatrix} \ddot{\xi}_0 \\ \ddot{\psi} \end{bmatrix} + \begin{bmatrix} c_\xi & 0 \\ 0 & 0 \end{bmatrix} \begin{bmatrix} \dot{\xi}_0 \\ \dot{\psi} \end{bmatrix} + \begin{bmatrix} e_r\Omega_0^2 S_\xi + k_\xi & 0 \\ 0 & 0 \end{bmatrix} \begin{bmatrix} \xi_0 \\ \psi \end{bmatrix} \right) = 0 \tag{47}$$

The coupling between the drive train and the collective lead-lag motion purely comes from the inertial loads.

The second block, consisting of two equations, the first pair of cyclic ones

$$\frac{N_b}{2} \left(\begin{bmatrix} J_{\xi\xi} & 0 \\ 0 & J_{\xi\xi} \end{bmatrix} \begin{bmatrix} \ddot{\xi}_{1c} \\ \ddot{\xi}_{1s} \end{bmatrix} + \begin{bmatrix} c_\xi & 2J_{\xi\xi}\Omega_0 \\ -2J_{\xi\xi}\Omega_0 & c_\xi \end{bmatrix} \begin{bmatrix} \dot{\xi}_{1c} \\ \dot{\xi}_{1s} \end{bmatrix} + \begin{bmatrix} e_r\Omega_0^2 S_\xi + k_\xi - J_{\xi\xi}\Omega_0^2 & c_\xi\Omega_0 \\ -c_\xi\Omega_0 & e_r\Omega_0^2 S_\xi + k_\xi - J_{\xi\xi}\Omega_0^2 \end{bmatrix} \begin{bmatrix} \xi_{1c} \\ \xi_{1s} \end{bmatrix} \right) = 0 \tag{48}$$

Considering only the Inertial, external Damping and centrifugal loads, the cyclic modes shows no influence on the stability of the drive train dynamics.

2.3.6 Addition of Mast and External loading

A commonly used idealization in torsional vibration analysis assumes a massless shaft with torsional stiffness K_m connecting discrete lumped inertias J_H&J_E and ψ_H&ψ_E are angular displacement of the disk H & E. This approach reduces the distributed system to a one-degree-of-freedom model, here **H** represents the Hub.
The corresponding shaft work done equation is,

$$W_{shaft} = \delta\psi_H\, J_H\, \ddot{\psi}_H + \delta\psi_E\, J_E\, \ddot{\psi}_E + \delta(\psi_H - \psi_E)\, K_m\, (\psi_H - \psi_E) \tag{49}$$

whose contribution to the generalized forces is

$$\begin{bmatrix} N_b J_{\xi\xi} & -N_b J_{\xi\psi} & 0 \\ -N_b J_{\psi\xi} & N_b J_{\psi\psi} + J_H & 0 \\ 0 & 0 & J_E \end{bmatrix} \begin{bmatrix} \ddot{\xi}_0 \\ \ddot{\psi}_H \\ \ddot{\psi}_E \end{bmatrix} + \begin{bmatrix} N_b c_\xi & 0 & 0 \\ 0 & 0 & 0 \\ 0 & 0 & 0 \end{bmatrix} \begin{bmatrix} \dot{\xi}_0 \\ \dot{\psi}_H \\ \dot{\psi}_E \end{bmatrix} + \begin{bmatrix} N_b(e_r\Omega_0^2 S_\xi + k_\xi) & 0 & 0 \\ 0 & K_m & -K_m \\ 0 & -K_m & K_m \end{bmatrix} \begin{bmatrix} \xi_0 \\ \psi_H \\ \psi_E \end{bmatrix} = \begin{bmatrix} f_{\xi_0} \\ 0 \\ 0 \end{bmatrix} \tag{50}$$

and $f_{\xi 0}$ is irrelevant for the stability problem.
This equation explicitly illustrates the coupling between the collective lead–lag motion and the torsional oscillation of the hub (or mast). This coupling originates purely from inertial effects and plays a significant role in shaping the modal characteristics of the rotor–drivetrain system, influencing both the natural frequencies and mode shapes associated with the coupled lead–lag and torsional dynamics.

2.4. Flexible Dynamics

The static rotor blade can be simplified as an Euler-Bernoulli cantilever beam. The blade is discretized into uniform cross-section continuous rotating beam elements. The rotation of the beam induces centrifugal and Coriolis forces. The free vibration equations of lagwise motion can be expressed as

$$\frac{\partial^2}{\partial r^2}\left(EI_{zz}(r)V''\right) - \frac{\partial}{\partial r}\left(P(r)V'\right) - m(r)\Omega^2 V + m(r)\ddot{V} = 0 \tag{51}$$

where $(.)' = \frac{\partial}{\partial r}$, EI_{zz} is the lagwise bending stiffness, m is the mass per unit span, P is the axial force resulting from the integration of the distributed centrifugal loads, $P(r) = \int_r^R m(r)\Omega^2(e_r + r)dr$, R is the rotor radius, Ω is the rotor angular velocity and e_r is the radius of the hub.
The weak form,

$$\int_e^R \delta V'' EI_{zz}(r)V'' + \delta V' P(r)V' - \delta V m(r)\Omega^2 V + \delta V m(r)\ddot{V}\ dr = 0 \tag{52}$$

By approximating the field variable V(r,t) with suitable Hermite shape functions.

3. Tilt Rotor Drive Train Configurations

Most existing tiltrotor aircraft employ a symmetric drivetrain configuration composed of two primary gearboxes connected through a cross-shaft. This interconnecting shaft enables continuous power transfer and maintains rotational synchronization between the two rotors. Additionally, a central gearbox linking both sides of the transmission system enhances operational safety by allowing power redistribution in the event of an engine failure.
The drive train configurations for tiltrotor aircraft can be divided into three types, characterized by the location of the engine's and what

portion of the rotor gearbox-engine assembly tilts.
The Following Data are taken from Ref [2]

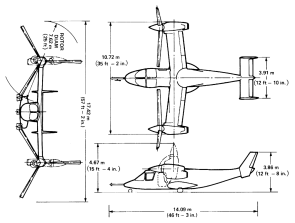

Figure 3: Three-view of the XV-15 Tiltrotor Research Aircraft.

The main structural data Ref. [2], namely the mass and chordwise stiffness distributions of each beam element of the discretized rotor blade are shown in Fig. 4.

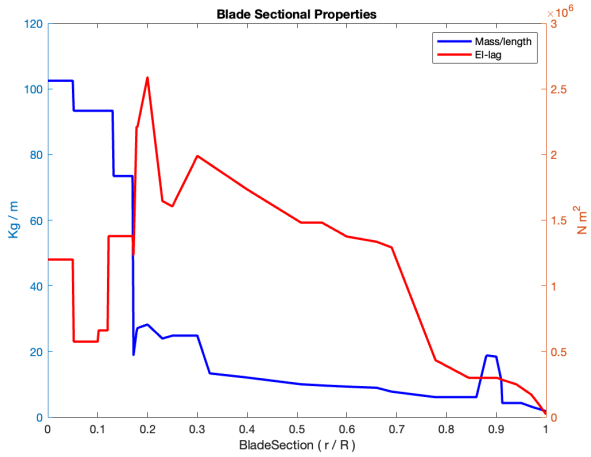

Figure 4: Blade Sectional Properties

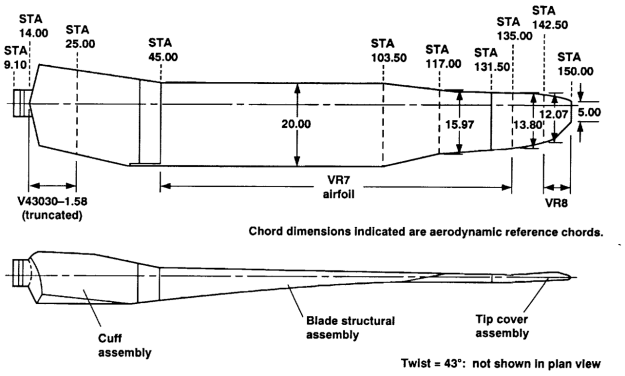

Figure 5: Planform and airfoil locations of the Advanced Technology Blade [All dimensions are in inches].

3.1. Configuration 1

In Configuration 1, the engine is located within the fuselage, while the rotors are mounted at the wingtips and are capable of tilting independently. This arrangement was characteristic of early tiltrotor prototypes, most notably the Bell XV-3, where a single fuselage-mounted engine transmitted power to the tip-mounted rotors through a series of gearboxes and interconnecting shafts. The primary advantage of this design lies in centralizing the engine mass, which simplifies maintenance and reduces weight at the wingtips. However, the long power transmission shafts introduce challenges, including torsional vibrations and additional structural requirements for the wings to withstand transmitted torque. In this configuration, only the rotors tilt to transition between vertical and horizontal flight, while the engine and fuselage remain fixed, necessitating precise synchronization of rotor speeds to maintain balanced lift and stability. Although largely superseded in modern tiltrotor aircraft, this configuration provided critical insights into power transmission, rotor control, and structural design that informed subsequent developments in tiltrotor technology.

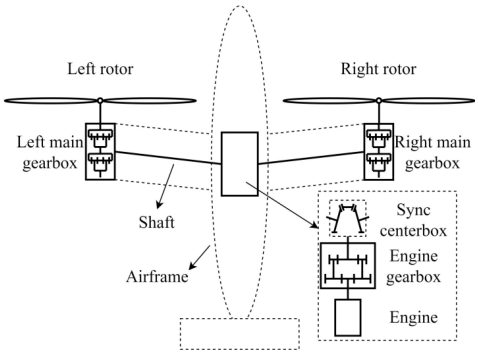

Figure 6: Skeleton

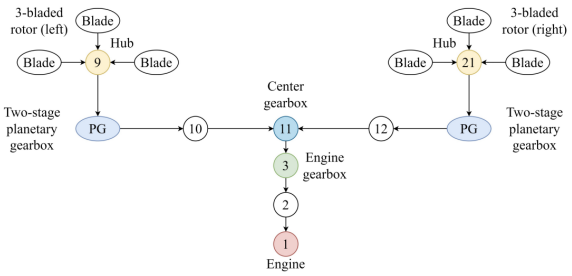

Figure 7: Topology figure of drive train

The images shown are adapted from Ref. [5].

No.	Element Type	Meaning
1	Rigid disk element	Engine
2	Massless shaft element	Engine shaft
3	Rigid disk element	Engine gearbox
11	Rigid disk element	Central gearbox
10, 12	Massless shaft element	Central shaft
PG	Rigid disk element	Two stage planetary gearbox
9, 21	Rigid disk element	Hub
n_1	Gear ratio	Two stage planetary gearbox
n_2	Gear ratio	Central gearbox
n_3	Gear ratio	Engine gearbox

Table 1: Meaning of the elements in topology figure presented in Fig. 7

3.1.1 Equivalent parameters

The equivalent inertia of a gear system represents the effective inertial property of multiple rotating components when referred to a common shaft. Due to the kinematic constraints imposed by gear ratios, the rotational speeds of interconnected gears are not independent; instead, they are related by the transmission ratio. As a consequence, the inertia of each gear must be scaled according to the square of its corresponding gear ratio when expressed with respect to a reference shaft. This transformation allows the entire gear train to be modeled as a single lumped inertial element, thereby simplifying dynamic analysis while preserving the system's kinetic energy equivalence.

$Je_9 = Je_{21} = J_{RotorHub}$	$Ke_{PG} = K_{PG}$
$Je_{PG} = J_{PG1} + J_{PG2}n_1^2$	$Ke_{12} = Ke_{10} = K_{10}n_1^2$
$Je_{11} = J_{11,1}n_1^2 + J_{11,2}n_1^2n_2^2 + J_{11,3}n_1^2$	$Ke_{EG} = K_{EG}n_1^2n_2^2$
$Je_{EG} = J_{EG1}n_1^2n_2^2 + J_{EG2}n_1^2n_2^2n_3^2$	$Ke_2 = K_2n_1^2n_2^2n_3^2$
$Je_E = J_En_1^2n_2^2n_3^2$	

Table 2: Equivalent Inertia and Stiffness tabulation

3.2. Configuration 2

In Configuration 2, the engines are mounted in nacelles at the wingtips, and both the engine nacelles and the rotors tilt together during transition between vertical and horizontal flight. This arrangement allows the power source to remain close to the rotors, significantly reducing the complexity and length of the drive train compared to fuselage-mounted engines. By tilting the entire nacelle, including the engine, this configuration minimizes the torsional loads on transmission components and improves mechanical efficiency. Additionally, it provides a more direct path for power transmission, reducing losses and the risk of vibration-induced fatigue in long shafts. Control of rotor speed and tilt angle is achieved through integrated nacelle and rotor actuation systems, which enable smooth transitions while maintaining lift symmetry and flight stability. This configuration has been widely adopted in modern tiltrotor aircraft, such as the Bell Boeing V-22 Osprey, due to its combination of mechanical simplicity, reliability, and performance efficiency.

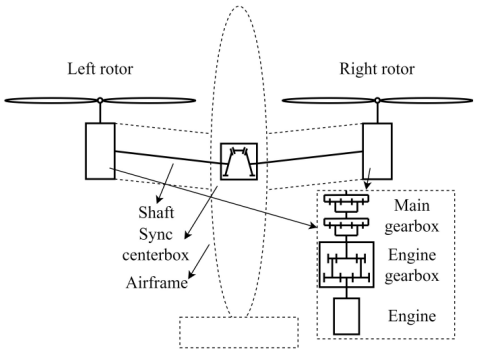

Figure 8: Skeleton

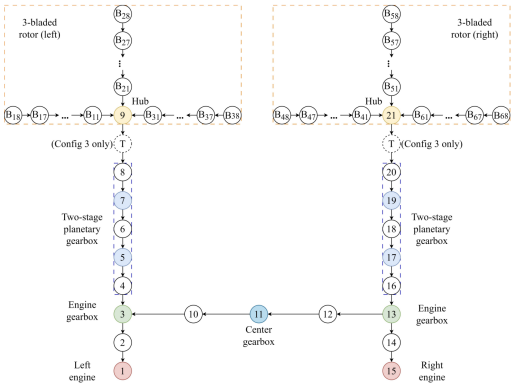

Figure 9: Topology figure of drive train

Figure 10: Configuration2

The images shown are adapted from Ref. [5].

No.	Element Type	Meaning
1, 1	Rigid disk element	Engine
2, 14	Massless shaft element	Engine shaft
3, 13	Rigid disk element	Engine gearbox
11	Rigid disk element	Central gearbox
10, 12	Massless shaft element	Central shaft
4-8, 16-20	Rigid disk element	Two stage planetary gearbox
9, 21	Rigid disk element	Hub
n_1	Gear ratio	Two stage planetary gearbox
n_2	Gear ratio	Central gearbox
n_3	Gear ratio	Engine gearbox

Table 3: Meaning of the elements in topology figure presented in Fig. 9

$$
\begin{aligned}
&Je_9 = Je_{21} = J_{RotorHub}^2 \\
&Je_{PG} = J_{PG1} + J_{PG2} n_1^2 \\
&Je_{11} = J_{11,1} n_1^2 n_2^2 + J_{11,2} n_1^2 n_2^2 n_4^2 + J_{11,3} n_1^2 n_2^2 \\
&Je_3 = Je_{13} = J_{3,1} n_1^2 + J_{3,2} n_1^2 n_2^2 + J_{3,3} n_1^2 n_3^2 \\
&Je_1 = Je_{15} = J_E n_1^2 n_3^2 \\
&Ke_{PG} = K_{PG} \\
&Ke_{EG} = K_{EG} n_1^2 \\
&Ke_{10} = Ke_{12} = K_{10} n_1^2 n_2^2 \\
&Ke_2 = Ke_{14} = K_2 n_1^2 n_3^2
\end{aligned}
$$

Table 4: Equivalent Inertia and Stiffness tabulation

4. Results and Validation

4.1. Gear System

The simple gear model is taken from Ref. [10]

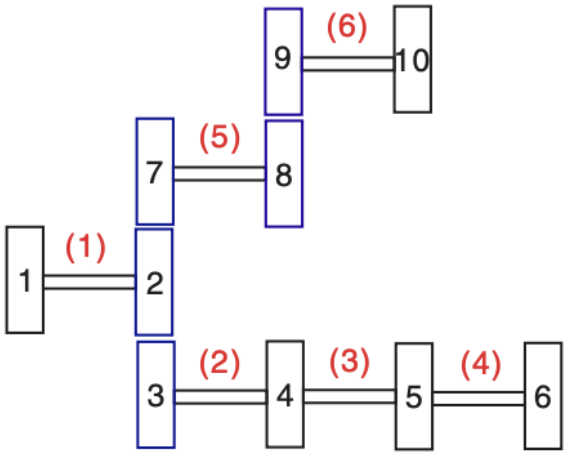

Figure 11: A typical tree system with two branches

Figure 11 shows the simplified torsional gear train used in this study. The system is modelled as a lumped-mass parameter branched drive-train composed of 10 rigid inertias (disks) connected by 6 torsional shafts.

Disk No.	**1**	**2**	**3**	**4**	**5**	**6**	**7**	**8**	**9**	**10**
I_i (kg·m^2)	1,098.21	111.45	4.07	45.42	26.44	26.44	0.41	33.90	0.04	9.22
Shaft No.	1	2	3	4	5	6				
k_i (N·m·rad^{-1})	616,897	196,594	3,986,105	7,762,058	219,191	242,917				
Gear ratios	$\frac{N_2}{N_3}$	$\frac{N_2}{N_7}$	$\frac{N_8}{N_9}$							
n_i	51/22	51/11	450/53							

Table 5: Moment of inertia and torsional stiffness of each component in the system

The branching is created by the geared connections, which split the power flow into two paths, producing a typical tree structure with multiple coupled rotational degrees of freedom. The inertial properties and shaft torsional stiffness values used in the model are summarised in Table 5.

4.1.1 Eigen Analysis

The constrained matrices have been formulated using the minimal coordinate set approach. The corresponding eigenvalues are listed below:

FEM	**Shaft mass**	Ω_1	Ω_2	Ω_3	Ω_4	Ω_5
Present	Neglected	23.0899	41.3224	217.5332	376.9099	713.1052
Ref [10]		23.0899	41.3228	217.6013	376.9155	712.6985

Table 6: Natural frequencies (rad/s) of the geared branch system

The predicted natural frequency results closely match the reference solution in Ref. [10], with extremely small differences (maximum relative deviation about 0.06%). This agreement validates both the modelling assumptions (lumped inertias, massless shafts, linear torsional springs) and the correct implementation of the geared constraints and ratio mapping in the system matrices.

4.1.2 Sensitivity Analysis

The following figures illustrate how variations in inertial and stiffness parameters influence a specific eigenmode. These results are presented as part of the eigen-sensitivity analysis.
Due to the gear constraints, inertial disks 2, 3, and 7 behave as a single rigid body. Likewise, disks 8 and 9 form another dynamically coupled unit. Nevertheless, the magnitude of the eigenvalue sensitivity is governed by the equivalent inertia of each coupled group and the corresponding gear ratios. Consequently, disks 2, 3, and 7 predominantly excite Mode 3, while disks 8 and 9 primarily excite Mode 5.

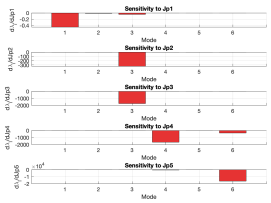

(a) Mass Sensitivity Chain 1.

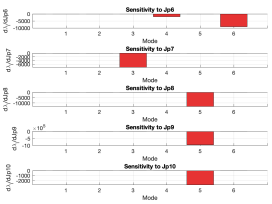

(b) Mass Sensitivity Chain 2.

Figure 12: Eigenvalue Sensitivity $[\frac{rad^2}{s^2}]$ to change in Polar Moment of Inertia (J_P).

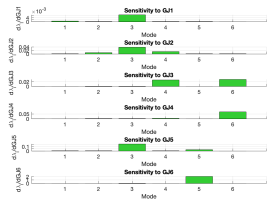

Figure 13: Eigenvalue Sensitivity $[\frac{rad^2}{s^2}]$ to change in Torsional Rigidity $(\frac{GJ}{l})$

Similarly, shafts 1, 2, and 5 are dynamically coupled. As they constitute the primary branch shafts of the system, they contribute to all vibration modes. However, their influence is most pronounced in Mode 3.

4.2. Lead-lag Collective & Hub torsional Coupling Validation

4.2.1 Numerical example

For the following mode shapes, the inertial moments arising from lead–lag dynamics induce oscillations in the drivetrain.

Segment	1	2	3	4	5	6
x_i (m)	[0.4, 0.7]	[0.7, 0.9]	[0.9, 1.1]	[1.1, 1.6]	[1.6, 5.2]	[5.2, 5.6]
m_0 (kg · m^{-1})	55	40	20	15	10	6
EI (N · m^2)	8×10^6	10×10^6	4×10^6	1.5×10^6	1×10^6	0.6×10^6

Table 7: Mass and lead–lag bending stiffness properties of the rotor blade

Results are validated with Adams for the following Blade model in Ref. [10], Modal analysis is performed using Eq. 50.

Components	units	Value
No. of blades		3
Hub Inertia J_H	(kg m^2)	10
Engine Inertia J_E	(kg.m^2)	10
Mast Stiffness GJ/l	(N.m.rad^{-1})	1e+5
Blade Root Spring Stiffness K_ξ	(N.m.rad^{-1})	2.4318e+06

Figure 14: numerical values of model parameters

RPM	Frequency	f1	f2
	Mode	Lead-Lag Collective and Hub Torsion (Coupling)	Lead-Lag Collective and Hub Torsion (Coupling)
0	**Present**	15.8238	76.7735
	Adams	15.8238	76.7735
200	**Present**	15.833	79.318
	Adams	15.833	79.318
350	**Present**	15.8482	84.1875
	Adams	15.8482	84.1875

Table 8: Natural Frequency, unit: (Hz), Cyclic modes are not tabulated

The system exhibits one low-frequency mode associated with hub oscillation, primarily governed by the rotor inertia $J_{\psi\psi}$. In contrast, a high-frequency mode is observed corresponding to the blade lead–lag motion, which is predominantly influenced by the lead–lag inertia $J_{\xi\xi}$. Further details regarding the coupling mechanism between collective and torsional dynamics are provided in Eq. 50. The coupling frequency depends on the angular velocity Ω of the rotor and the torsional stiffness of the mast and other rotor blade parameters. Considering the rotor parameters as constant, the following plots 4.2.2 and 4.2.3 presents the variation of the eigenvalues with respect to the dependent parameters. The eigenfrequencies identified in this study vary with rotational speed solely due to inertial and centrifugal effects.

Gyroscopic effects—arising from the coupling between lead–lag and flapping dynamics—are not considered, as they lie beyond the scope of the present work.

4.2.2 FanPlot: Hinged Blade

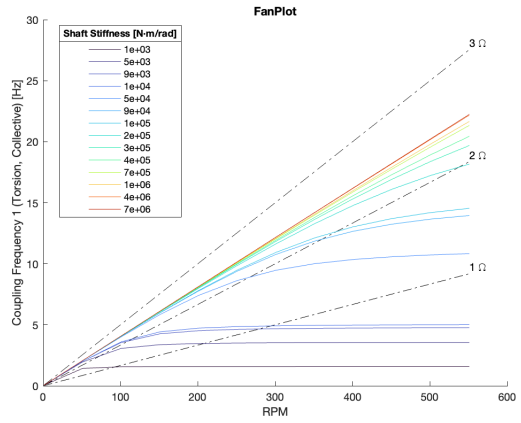

(a) Mode 1.

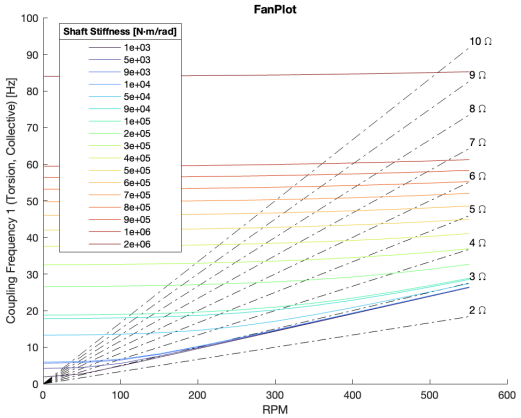

(b) Mode 2.

Figure 15: Eigen Plot

For Mode 1, the coupling frequency exhibits no variation with angular velocity, indicating a linear dependency resulting from the increased shaft stiffness. This mode is particularly critical, as intersections between the coupling frequency and excitation frequencies ($1\Omega, ...n\Omega$) are used to identify potential resonance conditions (critical speeds).

For Mode 2, the coupling frequency associated with lower torsional stiffness varies with angular velocity. However, increasing the torsional stiffness produces no noticeable response in this mode.

4.2.3 FanPlot: Hingeless Blade

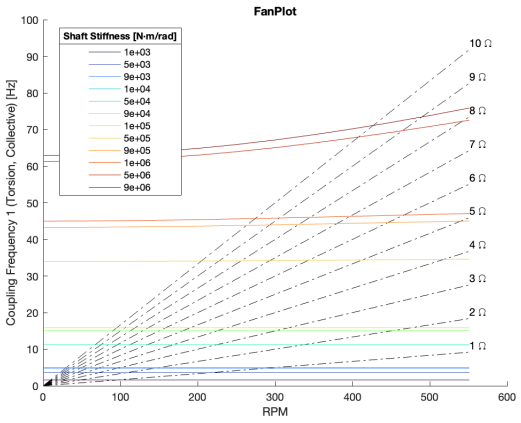

(a) Mode Hingeless 1.

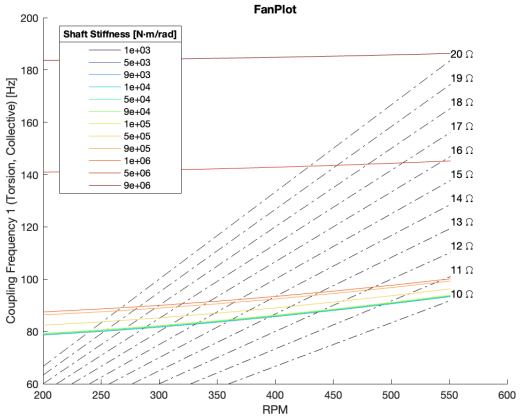

(b) Mode Hingeless 2.

Figure 16: Eigen Plot Hingeless

For Mode 1, behavior similar to the hinged-blade configuration is observed. However, a higher mast torsional stiffness is required to produce noticeable changes in the coupling frequency with increasing angular velocity. This is attributed to the added stiffness at the blade root.

For Mode 2, a mast with lower torsional stiffness can exhibit variations in coupling frequency as angular velocity increases. Even a slight increase in stiffness, however, renders the system sufficiently stiff that its response to angular velocity becomes negligible.

It is evident that at higher angular velocities, both configurations (hinged and hingeless) converge to nearly the same coupling frequency for lower torsional stiffness. This behavior is likely driven by the dominant effect of increased centrifugal forces.

For the following Tilt rotor eigen analysis flapping and airloads are not included, taken into consideration only the Collective-Torsional coupling.

5. Configuration

Table 9 compares the first four natural frequencies (f_1–f_4) of articulated and hingeless rotor blades at different rotational speeds. Results from the Transfer Matrix Method (TMM) and Finite Element Method (FEM) are shown side by side.

Mode (RPM)	Rotor	Method	f_1	f_2	f_3
0	Articulated	TMM	0	61.2676	153.9272
		FEM	0	61.2677	153.9312
	Hingeless	TMM	16.8468	90.2789	208.3165
		FEM	16.8469	90.2795	208.3223
565	Articulated	TMM	3.7084	63.8058	156.6721
		FEM	3.6825	63.7783	156.6842
	Hingeless	TMM	17.6077	92.5644	210.6676
		FEM	17.5836	92.5416	210.6897
458	Articulated	TMM	3.0005	62.9468	155.7364
		FEM	2.9845	62.9288	155.7444
	Hingeless	TMM	17.3357	91.7728	209.8796
		FEM	17.3357	91.7728	209.8796

Table 9: Natural frequencies (Hz) of the rotor blade for different rotational speeds

From the design point of view it is important to remove the rotor blade natural frequencies from the n/rev excitation frequencies over the normal rotor operating speed range. This ensures that the blades will be free of resonance under normal operating conditions. Both configurations listed below are symmetric, which leads to a symmetric eigenvalue problem. While symmetry simplifies the mathematical formulation and ensures real eigenvalues and orthogonal mode shapes, it also introduces challenges. In particular, closely spaced or repeated eigenvalues may occur, making mode identification and tracking difficult, especially when parameters such as stiffness or angular velocity are varied. Additionally, numerical sensitivity can arise, requiring careful discretization and solver selection to accurately capture the coupled dynamic behavior. The results of Configuration 2 are presented first, as its architectural design corresponds to the current configuration of the XV-15 tiltrotor

5.1. Configuration 2

Equivalent inertia of each component, and equivalent torsional stiffness of each component's output shaft, Gear ratios in the drive train system are given in Table 11, 10 respectively.

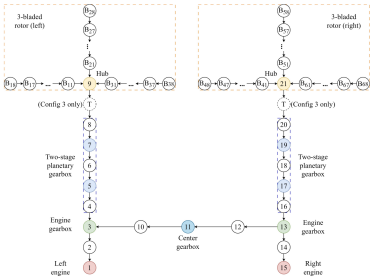

Figure 17: Topology figure of drive train

Components	Gear Ratio
Engine - Engine gearbox (n_3)	19846:8487
Engine gearbox - Planetary gearbox (n_1)	8487:565
Engine gearbox - Center gearbox (n_2)	8487:6392

Table 10: Gear ratios for Drive Train Configuration 2.

Mode	Properties (Equivalent)	Engine	Engine Gearbox	Central Gearbox	Planetary Gearbox	Rotor Hub
Helicopter & Airplane	**Inertia** ($Kg.m^2$)	9.82	1.96	0.6	3.68	7.38
	Torsional Stiffness GJ($N.m.rad^{-1}$)	168e4	41.7e4	3.17e4	8.48e4	-

Table 11: Properties of each component in Drive Train Configuration 2

Method	f1	f2	f3	f4	f5	f6
FEM (Without Rotor)	5.75	19.20	19.78	51.94	60.35	60.36

Table 12: Natural frequency of Drive Train without Rotor, unit: (Hz)

The proposed drivetrain system modeling and analysis approach is validated by comparing the simulation results of Configuration 2 with published test data in the literature Ref. [7] [3].

Mode	Model (Method)	f1	f2	f3	f4
RPM = 565 Helicopter Mode	Ref. [7]	3.67	11.87	13.47	32.21
	Rigid Blade (FEM)	1.035	11.029	13.252	59.971
	Flexible Blade (FEM)	-	11.009	13.234	47.4378
RPM = 458 Airplane Mode	Ref. [7]	3.66	11.83	13.43	32.21
	Rigid Blade (FEM)	1.035	11.023	13.248	59.963
	Flexible Blade (FEM)	-	11.009	13.234	46.9728

Table 13: Natural frequency of Drive Train, unit: (Hz)

It can be found that the results obtained by the Rigid blade method in Table 13, closely align

with both the test data and results from flexible blade at low frequencies, thereby illustrating the effectiveness of the proposed method.
The key outcome of the eigenanalysis is the identification of critical rotational RPM corresponding to shaft resonances and self-excited vibrations. To facilitate this, a comprehensive set of charts has been generated Fig. 18, illustrating these critical values across a broad spectrum of physical parameters.

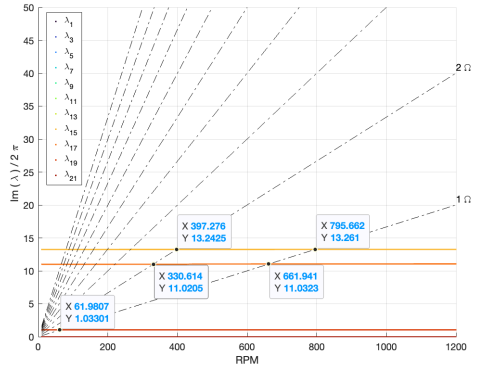

(a) Rigid Hingeless Blade.

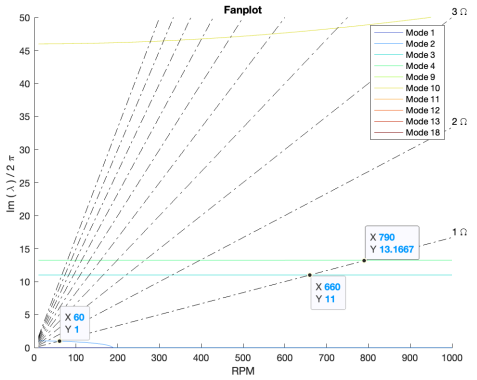

(b) Flexible Hingeless Blade.

Figure 18: Campbell diagram: Configuration 2

The reduction of the first lag natural frequency of the flexible blade to zero with increasing rotational speed is caused by linear centrifugal softening, where the distributed spin-induced term $-m\Omega^2 V$ (Ref. 51) acts as negative geometric stiffness and progressively cancels the elastic bending stiffness. When the effective stiffness vanishes, the corresponding eigenvalue satisfies $\omega^2 = 0$, indicating a loss of static stability (divergence-type instability).
Due to the idealized assumptions of perfectly aligned shafts and lumped mass representation, the real part of the eigenvalues at the critical rotational speeds indicates no instability. However, in practical applications, shaft mass eccentricity or offset may introduce destabilizing effects, potentially leading to instability near the resonant frequencies.

5.1.1 Eigen Modes

The following figures illustrate the dynamic behavior of the drivetrain, including the symmetrical and asymmetrical response patterns of the system, the rotor hub responses, and the collective lead–lag motion of the blades, the relative torsional deformation of each element within the drivetrain gear system are presented at the corresponding natural frequencies associated with the helicopter mode at 565 rpm. These results are used to examine the in-phase and out-of-phase motion of the individual drivetrain components.
For the flexible case, the plots show the mode shapes as functions of the blade radial coordinate. Blades 1, 2, and 3 belong to Rotor 1, whereas Blades 4, 5, and 6 correspond to Rotor 2, illustrating the variation of the lead-lag deflection along the blade radial position.
The overlapping responses of the blades within each rotor (Blades 1–3 for Rotor 1 and Blades 4–6 for Rotor 2) indicate the presence of collective blade modes, where the blades of a given rotor move in phase. Furthermore, when considering the rotors as complete assemblies, overlapping responses between Rotor 1 and Rotor 2 signify Asymmetric mode patterns, whereas non-overlapping responses indicate Symmetric modes, corresponding to out-of-phase motion between the two rotors Ref. [7].

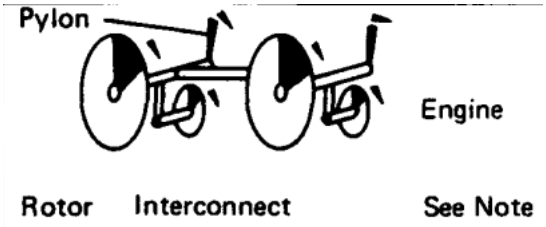

(a) Asymmetrical Mode shape.

(b) Symmetrical Mode shape.

Figure 19: Mode shape of drive train system configuration 2

5.1.2 Asymmetric Mode shape

These involve opposite or differential motion between the left and right sides. For example, one rotor shaft twists one way while the opposite shaft twists the other, producing relative motion across the centerline as shown in Fig. 19a.

5.1.3 Symmetric Mode shape

These involve motions where left and right drivetrain and rotor components move in unison — that is, both sides twist, bend, or oscillate the same way relative to the aircraft centerline (mirror motion across the centerline). There is no differential torque or deflection between left and right systems in these modes as shown in Fig. 19b.

5.1.4 Mode Shapes for Drive train natural frequencies

In the illustrated configuration:

- PG1 and PG2 denote the output shafts of the Planetary gears 1 & 2 respectively.
- EG1 and EG2 denote the output shafts of the Engine gears 1 & 2 respectively.
- E1 and E2 denote the output shafts of Engine 1 & Engine 2 respectively.
- CG1 and CG2 denote the output shafts of the central gear assemblies.

The system consists of two independent transmission chains:

- **Chain 1** comprises Rotor 1 (Blade 1, Blade 2, and Blade 3), PG1, EG1, and E1.
- **Chain 2** comprises Rotor 2 (Blade 4, Blade 5, and Blade 6), PG2, EG2, and E2.

Each chain represents a complete power transmission path from the corresponding engine output shaft to the associated rotor assembly.
The first in-plane mode of the flexible blade decreases and eventually approaches zero as the rotational speed increases due to centrifugal softening. To ensure a meaningful comparison with the rigid-blade model, the results at a lower rotational speed (100 rpm) are therefore considered. In contrast, the first natural frequency of the rigid-blade model remains nearly invariant with respect to rotational speed, as the rigid formulation does not include distributed spin-softening effects.
For the following analysis, the eigenmode of the hinged rigid blade without root damping is presented in Fig. 23a. This figure serves as a reference for comparing mode shapes and illustrates how the introduction of blade stiffness alters the characteristics of the drivetrain torsional oscillations and the collective lead–lag response.

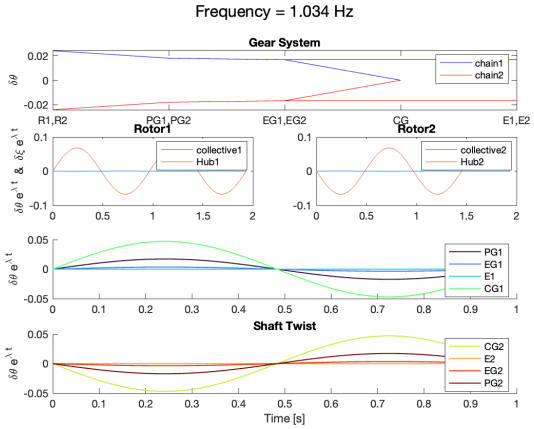

(a) Hingeless Blade.

Figure 20: Rigid Blade.

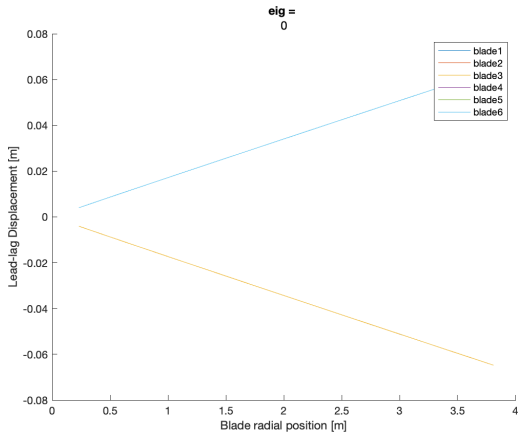

(a) Rotor.

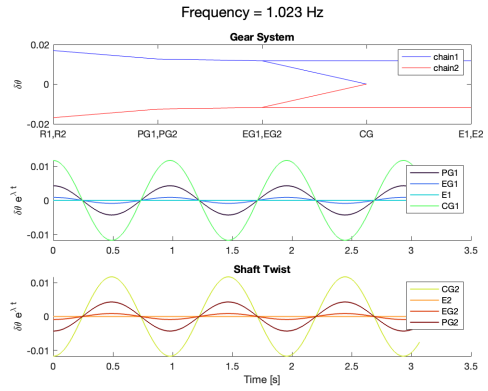

(b) Drive Train Elements.

Figure 21: Flexible Hingeless Blade.

Figure 22: First Symmetrical Mode (rpm 100).

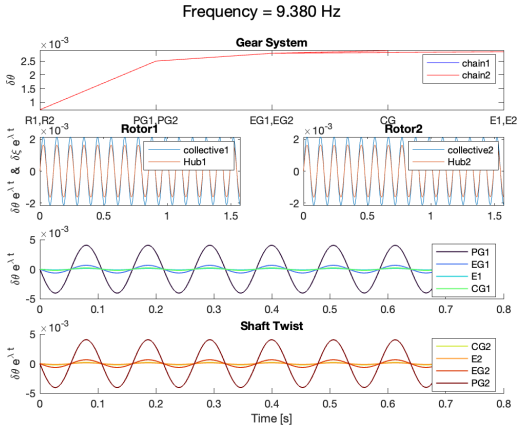

(a) Hinged Blade.

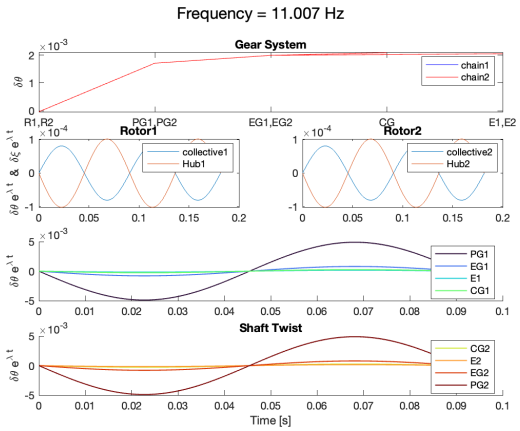

(b) Hingeless Blade.

Figure 23: Rigid Blade.

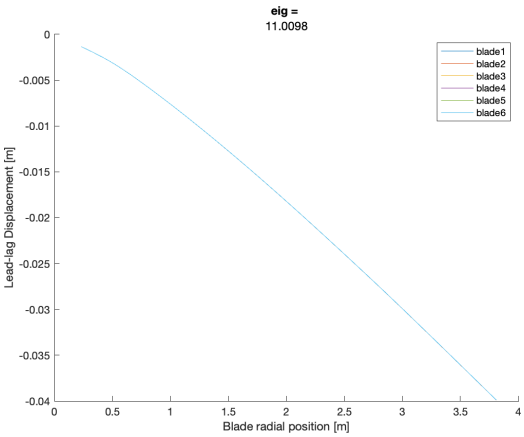

(a) Rotor.

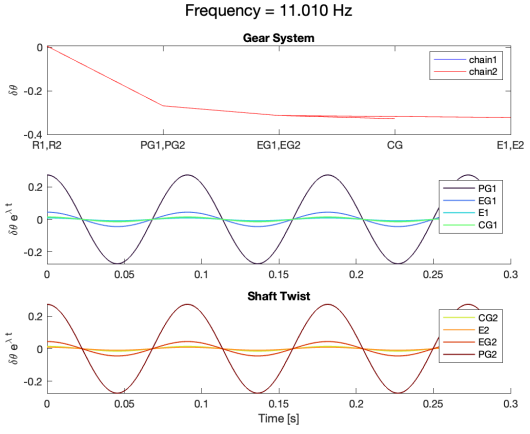

(b) Drive Train Elements.

An important observation from the first mode is that, at low frequencies, the collective blade motion and hub motion occur in anti-phase. As the frequency increases, this phase relationship gradually shifts toward in-phase motion for the hinged configuration.
The introduction of blade stiffness reduces this anti-phase behavior and results in lower lead–lag and hub oscillation amplitudes. Moreover, the corresponding mode shapes exhibit the same characteristics as those described in Section Asymmetric Mode 5.1.2.
At higher modal frequencies, the amplitude of the collective response increases and becomes in phase with the hub motion. In comparison with the first symmetric mode, the planetary shaft and the central shaft exhibit out-of-phase resonance, accompanied by an increase in oscillation amplitude.
Analysis of the drivetrain reveals that, at higher frequencies, the planetary shaft, the central shaft and Engine gear shaft oscillate in-phase and the relative torsional twist of the planetary shafts is higher compared to the central shafts.

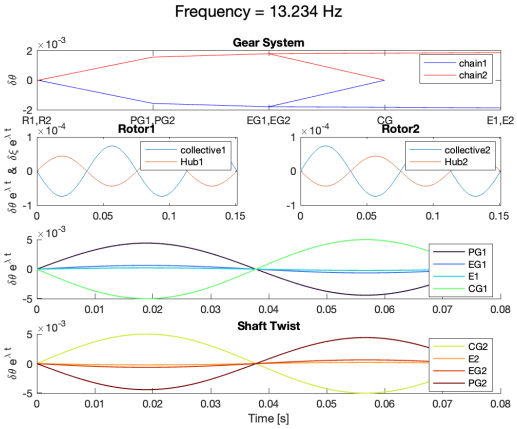

(a) Blade.

Figure 26: Rigid Hingeless Blade.

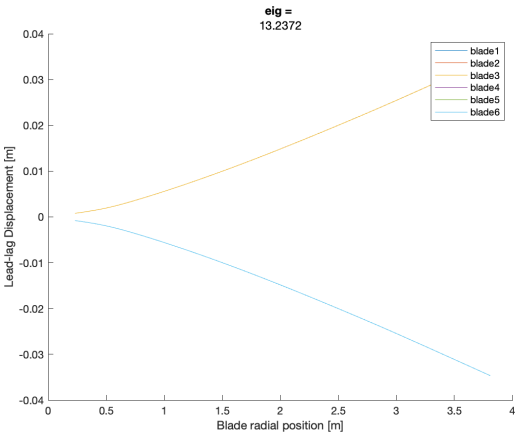

(a) Rotor.

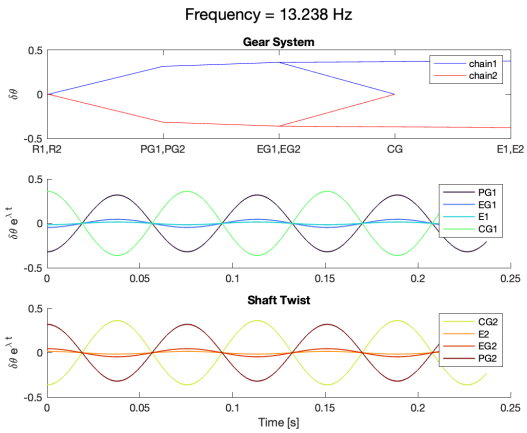

(b) Drive Train Elements.

Figure 27: Flexible Hingeless Blade.

Figure 28: Symmetrical Mode (rpm 565).

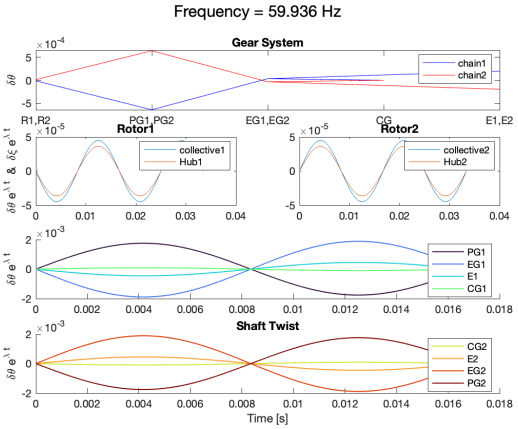

(a) Symmetrical Mode.

Figure 29: Hingeless Rigid Blade.

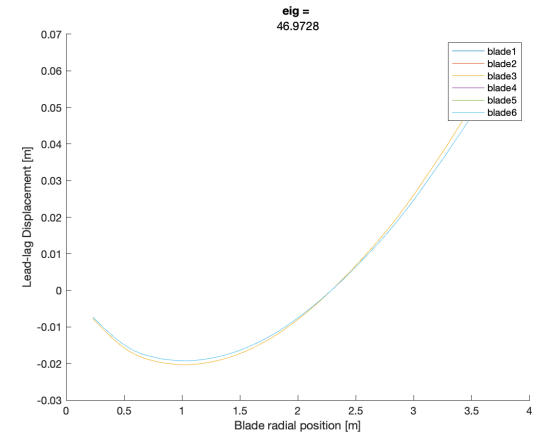

(a) Rotor.

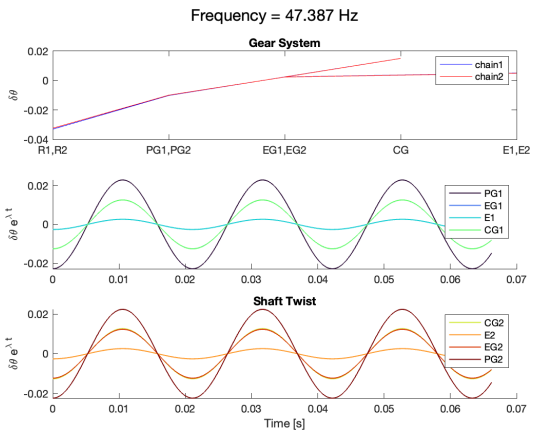

(b) Drive Train Elements.

Figure 30: Flexible Hingeless Blade (Asymmetrical Mode).

Figure 31: Mode Shapes (rpm 565).

5.1.5 Sensitivity Analysis of the Drive System

Variations in the rotational speed Ω_0 do not significantly affect the sensitivity of the eigenvalues with respect to the other drivetrain components.

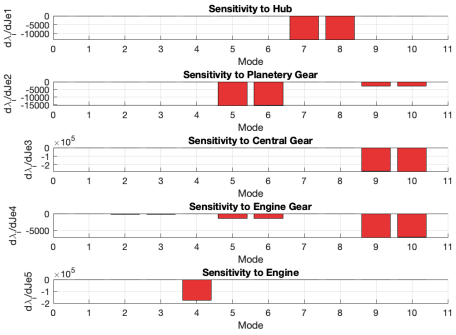

(a) Chain 1.

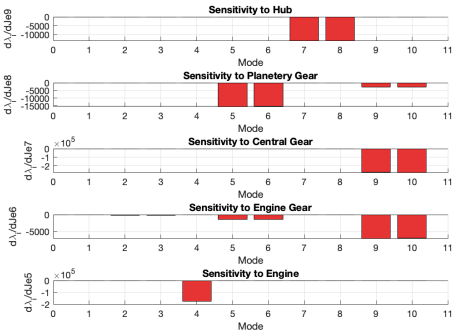

(b) Chain 2.

Figure 32: Eigenvalue Sensitivity $[\frac{rad^2}{s^2}]$ to change in Polar Moment of Inertia.

The eigenvalue sensitivity analysis chart indicates that the first mode remains unaffected by variations in other drivetrain inertial parameters, as it is governed solely by the rotor inertia $J_{\psi\psi}$ as shown in Eq. 50.

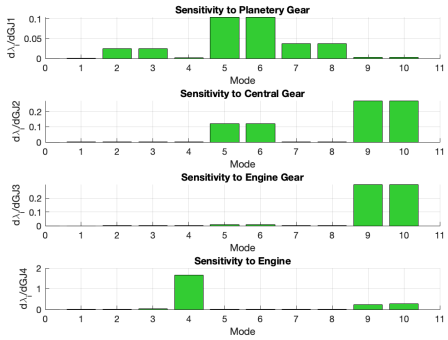

(a) Chain 1.

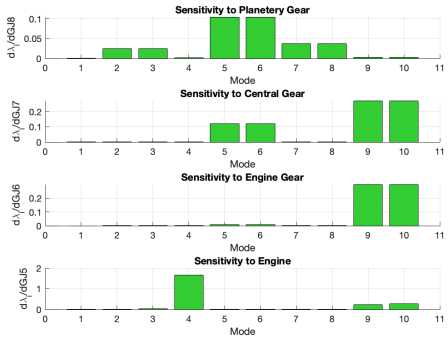

(b) Chain 2.

Figure 33: Eigenvalue Sensitivity $[\frac{rad^2}{s^2}]$ to change in Torsional Rigidity of the shafts.

Since the engine gearbox mechanically couples the planetary, engine, and central gear stages, its inertia and output shaft stiffness exert significant influence on the higher eigenmodes. Mode 4 is primarily dependent on the engine inertia and the stiffness of its output shaft.
Eigenmodes 6 and 7 exhibit pronounced sensitivity to the collective lead–lag inertia $J_{\xi\xi}$ and stiffness k_ξ as illustrated in Fig. 34. In addition to the lead–lag parameters, these modes are also significantly influenced by the inertia of the planetary and central gears, as well as by the torsional stiffness of their respective output shafts. As discussed in Section 4.2.3, rotor blade–dependent modes are affected not only by blade properties but also by the dynamic characteristics of the shafts that connect them to the transmission system. In the present configuration, this coupling is primarily governed by the planetary shaft, which plays a critical role in transmitting torsional interactions between the rotor and the drivetrain.

5.1.6 Effect of Damping

Root blade lead–lag dampers are incorporated into the rotor (rigid blade) model to examine the influence of damping variation on the modal characteristics of the system. The corresponding Damped frequency ω_d for different magnitudes of lead–lag damping are presented in Fig. 34.
At lower levels of damping, a mild reduction in the eigenfrequencies of Modes 6 and 7 is observed following the introduction of root lead–lag dampers (indicated by the blue curve starting at approximately 100 Hz). Modes 6 and 7 are rotor-dependent, with each mode primarily associated with one of the two rotors, reflecting their localized lead–lag dynamics. For higher damping values, for instance $Damping = 4000$ units, both modes exhibit a significant decrease in eigenfrequencies at low rotational speeds. As the rotational velocity increases, the frequencies gradually rise due to the dominant effect of centrifugal stiffening.
This behavior demonstrates that these rotor-dependent modes are highly sensitive to lead–lag parameters, including damping and inertia, and that their dynamic characteristics are strongly influenced by both the magnitude of damping and the rotational speed.

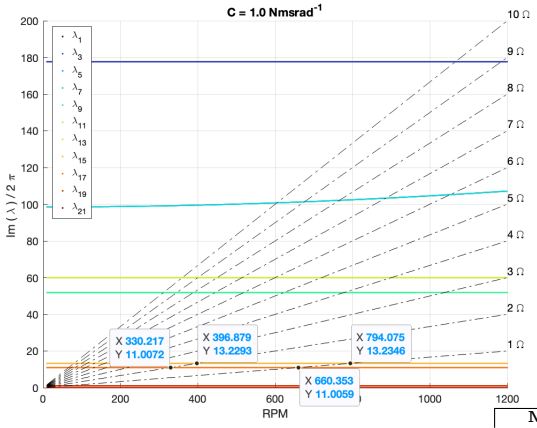

(a) C = 1.0 $Nms\ rad^{-1}$

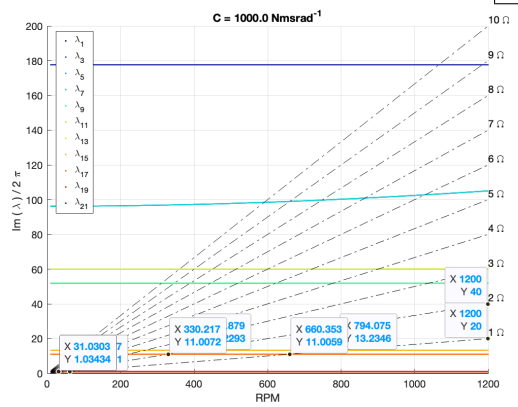

(b) C = 1000.0 $Nms\ rad^{-1}$

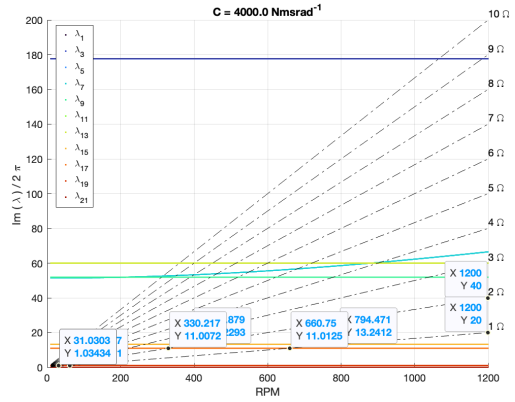

(c) C = 4000.0 $Nms\ rad^{-1}$

Figure 34: Damped frequency ω_d (Hz) plot for Varying Lead–Lag Damping

5.2. Configuration 1

Gear ratios, equivalent inertia of each component, and equivalent torsional stiffness of each component's output shaft in the drive train system are given in Table 14, 15 respectively.

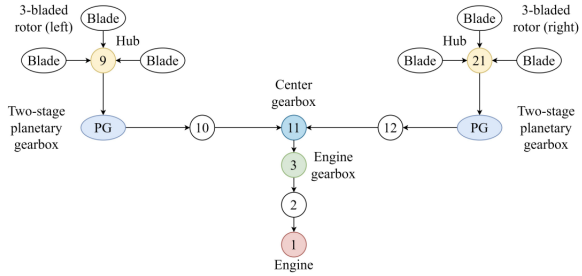

Figure 35: Topology figure of drive train

Mode	Properties (Equivalent)	Engine	Engine Gearbox	Central Gearbox	Planetary Gearbox	Rotor Hub
Helicopter & Airplane	**Inertia** $(Kg.m^2)$	19.64	1.96	0.6	3.68	7.38
	Torsional Stiffness GJ$(N.m.rad^{-1})$	337e4	41.7e4	3.17e4	8.48e4	-

Table 14: Properties of each component in drive train Configuration 1.

Components	Gear Ratio
Engine - Engine gearbox (n_3)	19846 : 8487
Engine gearbox - Center gearbox (n_2)	8487 : 6392
Center gearbox - Planetary gearbox (n_1)	6392 : 565

Table 15: Gear ratios for drive train Configuration 1.

Method	f1	f2	f3	f4	f5	f6
FEM (Without Rotor)	7.85	10.36	31.88	32.12	134.83	235.28

Table 16: Natural frequency of the Drive Train without Rotor, unit: (Hz)

The proposed drivetrain system modeling and analysis approach (the Multiblade Coordinate rigid-blade model) is validated against both the Finite Element Method (FEM) and the Transfer Matrix Method (TMM), as summarized in Table 17. Additional details regarding the TMM formulation and its implementation are provided in Appendix **??**.

Mode	Model (Method)	f1	f2	f3	f4
RPM = 565 Helicopter Mode	Rigid Blade (FEM)	1.069	6.874	28.0	28.268
	Flexible Blade (FEM)	-	6.871	27.9299	28.1883
	Flexible Blade (TMM)	-	5.1393	27.7908	27.9241
RPM = 458 Airplane Mode	Rigid Blade (FEM)	1.069	6.873	27.988	28.256
	Flexible Blade (FEM)	-	6.871	27.9178	28.183
	Flexible Blade (TMM)	-	5.1685	27.7707	27.9036

Table 17: Eigen Analysis, unit: (Hz)

The addition of rotors reduces the operating frequency of the gear system. In the following analysis, Flexible hingeless blades results are also shown. All cyclic modes and modes without torsional–collective coupling are excluded.

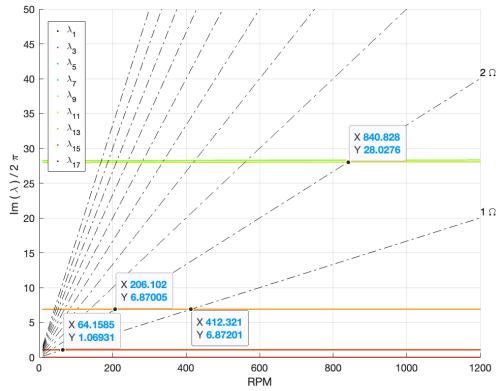

(a) Rigid Hingeless Blade.

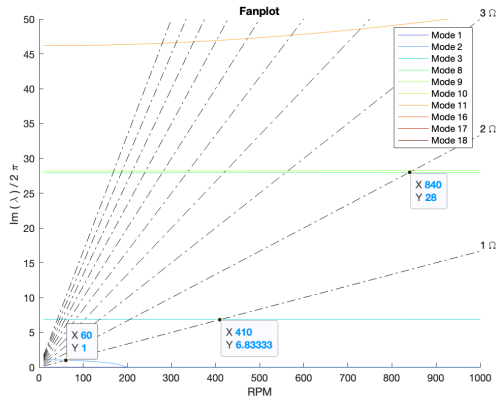

(b) Flexible Hingeless Blade.

Figure 36: Campbell diagram: Configuration 1

The reduction of the first lag natural frequency of the flexible blade to zero with increasing rotational speed is caused by linear centrifugal softening, where the distributed spin-induced term $-m\Omega^2 V$ (Ref. 51) acts as negative geometric stiffness and progressively cancels the elastic bending stiffness. When the effective stiffness vanishes, the corresponding eigenvalue satisfies $\omega^2 = 0$, indicating a loss of static stability (divergence-type instability).

5.2.1 Eigen Modes Shapes for Drive train natural frequencies

The following figures illustrate the dynamic behavior of the drivetrain, including symmetrical and asymmetrical response patterns, rotor hub responses, and collective lead–lag motion of the blades. The relative torsional deformation of each drivetrain element is shown at the natural frequencies corresponding to the helicopter mode at 565 rpm, highlighting in-phase and out-of-phase motion of individual components.

For the flexible case, mode shapes are plotted along the blade radial coordinate. Blades 1–3 belong to Rotor 1, and Blades 4–6 to Rotor 2, showing the variation of lead-lag deflection. Overlapping responses within a rotor indicate collective blade modes, while overlapping or non-overlapping responses between rotors correspond to asymmetric or symmetric modes, respectively [7] & [4].

Eigenanalysis reveals both symmetric and asymmetric mode shapes, which are discussed in detail in Section 5.1.3.

In the illustrated configuration:

- PG1 and PG2 denote the output shafts of the Planetary gears 1 & 2 respectively.
- CG1 and CG2 denote the output shafts of the Central gear.
- EG denote the output shafts of the Engine gear.
- E denote the output shafts of Engine.

The system consists of two independent transmission chains:

- **Chain 1** comprises Rotor 1 (Blade 1, Blade 2, and Blade 3), PG1, CG1, EG, and E.
- **Chain 2** comprises Rotor 2 (Blade 4, Blade 5, and Blade 6), PG2, CG2, EG, and E.

Each chain represents a complete power transmission path from the corresponding engine output shaft to the associated rotor assembly.

The first in-plane mode of the flexible blade decreases and eventually approaches zero as the rotational speed increases due to centrifugal softening. To ensure a meaningful comparison with the rigid-blade model, the results at a lower rotational speed (100 rpm) are therefore considered. In contrast, the first natural frequency of the rigid-blade model remains nearly invariant with respect to rotational speed, as the rigid formulation does not include distributed spin-softening effects.

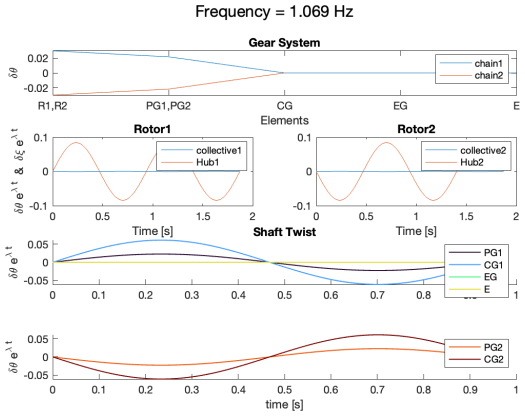

(a) Hingeless Blade.

Figure 37: Rigid Blade.

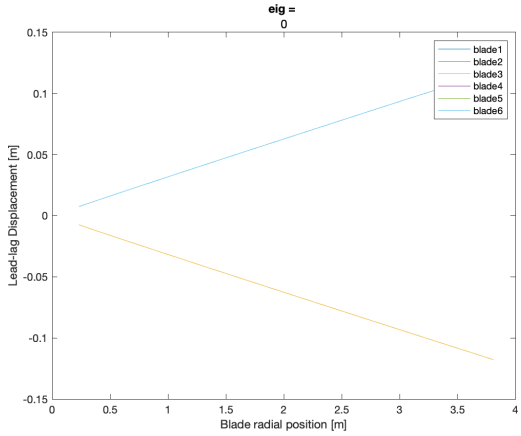

(a) Rotor.

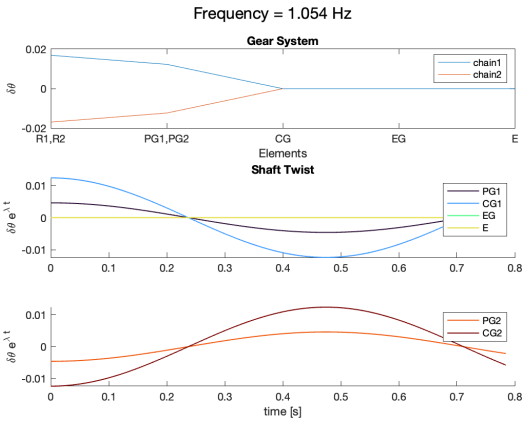

(b) Drive Train Elements.

Figure 38: Flexible Hingeless Blade.

Figure 39: First Symmetrical Mode (rpm 100).

A consistent modal trend is also observed in Configuration 1. In the low-frequency regime, the central shaft exhibits a larger vibration amplitude than the planetary shafts, indicating its dominant participation in the fundamental mode. Moreover, the shafts predominantly vibrate in phase, confirming that the first mode corresponds to a global synchronous motion of the drivetrain system.

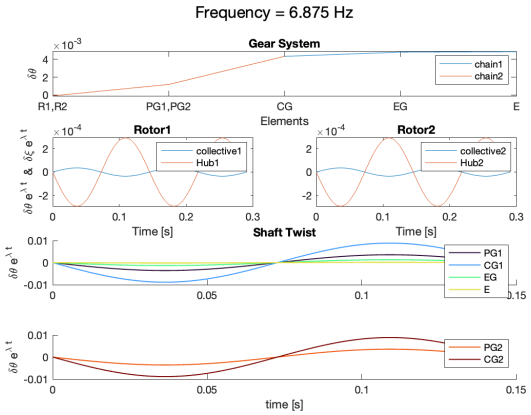

(a) Hingeless Blade.

Figure 40: Rigid Blade.

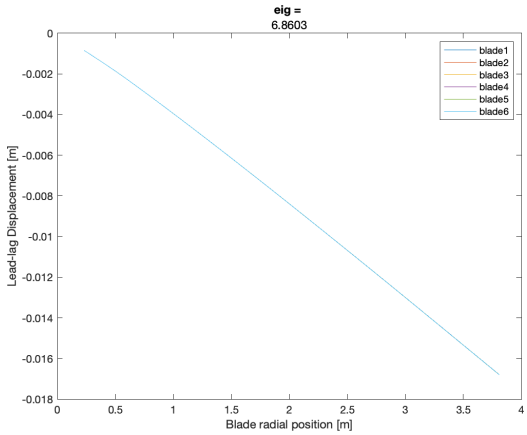

(a) Rotor.

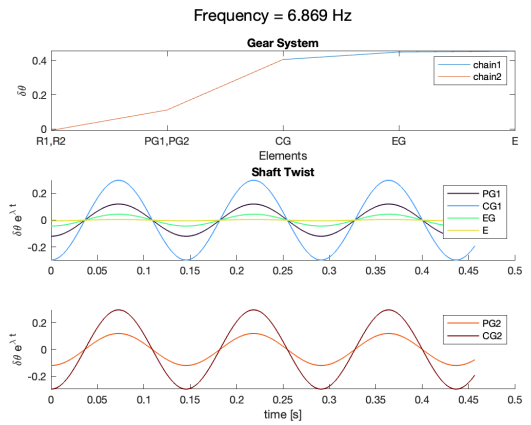

(b) Drive Train Elements.

Figure 41: Flexible Hingeless Blade.

Figure 42: First Asymmetrical Mode (rpm 565).

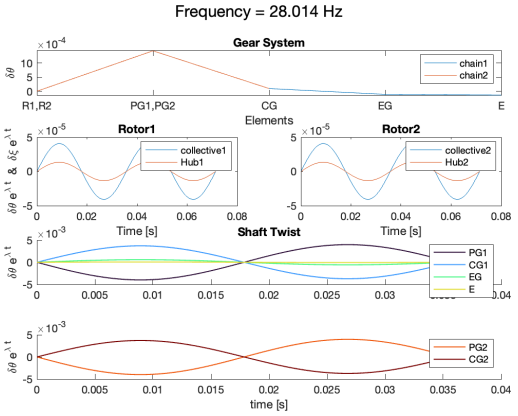

(a) Hingeless Blade.

Figure 43: Rigid Blade.

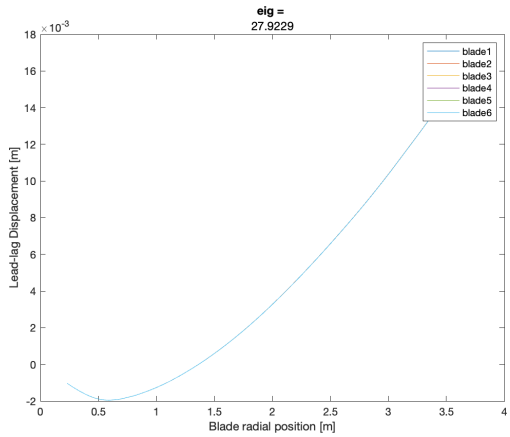

(a) Rotor.

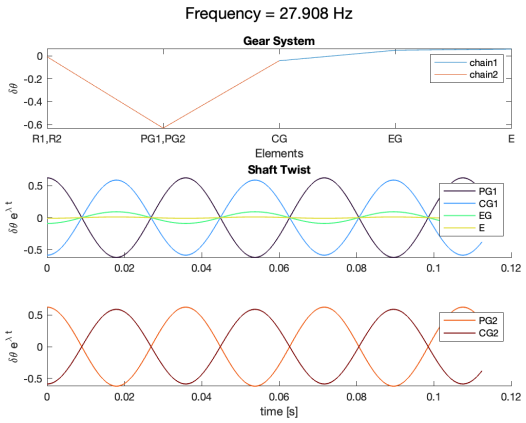

(b) Drive Train Elements.

Figure 44: Flexible Hingeless Blade.

Figure 45: Asymmetrical Mode (rpm 565).

An important observation from the first mode is that the lead–lag collective motion and the hub motion occur in anti-phase at low frequencies, indicating a dominant relative motion between the rotor and hub assembly. As the frequency increases, this phase relationship gradually transitions toward in-phase behavior, suggesting a redistribution of modal participation within the system. Simultaneously, the planetary shaft amplitude increases significantly and begins to oscillate out of phase with the central shaft, with both shafts exhibiting nearly equal magnitudes. This behavior reflects stronger dynamic coupling within the drivetrain and indicates a shift from a predominantly centralized mode to a more distributed modal response involving multiple shafts.
The engine gearbox shaft exhibits small oscillations in the asymmetrical mode and remains essentially stationary in the symmetrical mode.

5.2.2 Sensitivity Analysis of the Drive System with Rigid blade

Variations in the rotational speed Ω_0 do not significantly affect the sensitivity of the eigenvalues with respect to the other drivetrain components.

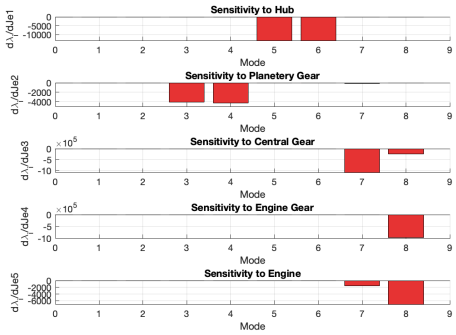

(a) Chain 1.

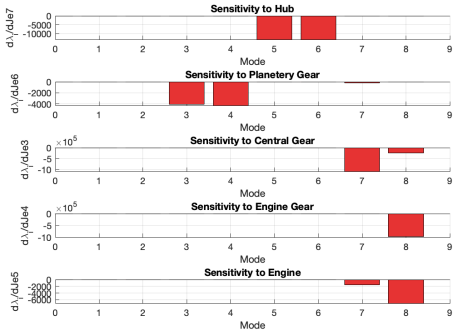

(b) Chain 2.

Figure 46: Eigenvalue Sensitivity $[\frac{rad^2}{s^2}]$ to change in Polar Moment of Inertia.

Same like the configuration 2, the first two modes are sensitive to rotor parameters $J_{\psi\psi}$ and

show a little sensitivity towards the planetary shaft (as discussed in section 4.2.3) and the central shafts.

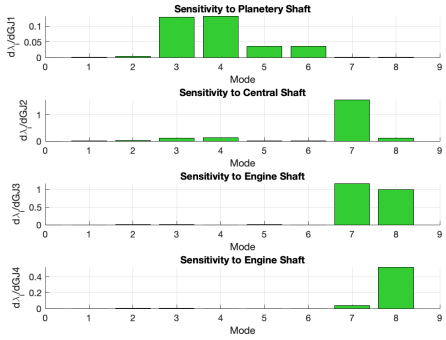

(a) Chain 1.

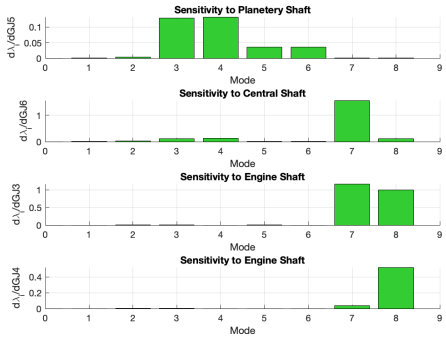

(b) Chain 2.

Figure 47: Eigenvalue Sensitivity $[\frac{rad^2}{s^2}]$ to change in Torsional Rigidity of the Gear and Engine shaft.

Modes 3 and 4 are predominantly influenced by the inertia and stiffness of the planetary gears, with only minor sensitivity to the central gear parameters, reflecting their higher participation in localized planetary dynamics. Modes 5 and 6 correspond to the collective lead–lag motions and are mainly governed by the rotor parameters, hub inertia, and planetary shaft stiffness, indicating strong coupling between the rotor and drivetrain in these modes. Since the engine and engine gearbox initiate power transmission through the system, they contribute more significantly to the higher-frequency modes, where their dynamic participation affects the overall modal response of the drivetrain.

5.2.3 Effect of Damping

Root blade lead–lag dampers are incorporated into the rotor (rigid blade) model to examine the influence of damping variation on the modal characteristics of the system. The corresponding Damped frequency ω_d for different magnitudes of lead–lag damping are presented in Fig. 48.

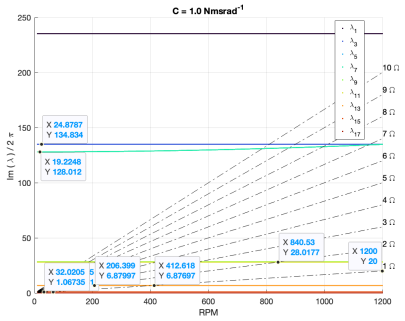

(a)

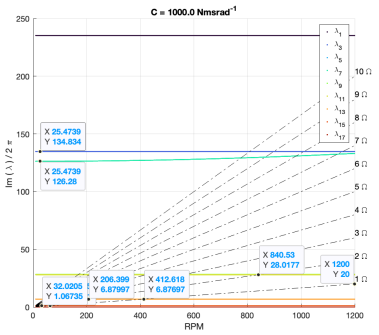

(b)

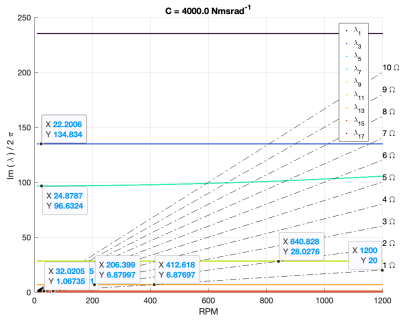

(c)

Figure 48: Damped frequency ω_d plot for Varying Lead–Lag Damping

Modes 5 and 6 form a pair of nearly identical eigenfrequencies, each corresponding to one of the two rotors. These modes are strongly governed by the collective lead–lag parameters and represent higher-frequency dynamic behavior. The introduction of root lead–lag dampers re-

sults in a noticeable increase in damping specifically in these modes, while only marginal and barely perceptible changes are observed in the remaining modes, indicating limited coupling with other dynamic components.
Furthermore, the influence of angular velocity is significant. As the rotational speed increases, centrifugal stiffening enhances the effective blade stiffness, leading to an upward shift in the associated natural frequencies. Consequently, at lower angular velocities, Modes 5 and 6 exhibit more pronounced damping effects due to their strong dependence on lead–lag dynamics. However, with increasing angular velocity, these modes progressively shift toward higher frequencies, and the relative impact of the added damping becomes less dominant.

6. Comparsion of Drive Train configurations

Taking into account the initial operating frequencies of both configurations, the root-mean-square (RMS) torque in each shaft has been computed and plotted for the eigenfrequencies of the two configurations for comparative analysis.
All lumped masses and shafts are assumed to oscillate with respect to the blade reference frame, so that torque is transmitted directly from the rotor blades to the drivetrain. In comparison to Configuration 1, the central gear shaft in Configuration 2 experiences lower torque, whereas the planetary gear shafts in Configuration 2 are subjected to higher torque relative to Configuration 1. This behavior is primarily due to the difference in power transmission paths: in Configuration 1, the primary chain originates from the engine and its gearbox, causing the associated shafts to carry significantly higher torque loads.
The observed differences highlight the importance of torsional load distribution in drivetrain design, as the torque experienced by individual shafts directly affects component sizing, fatigue life, and overall system reliability.

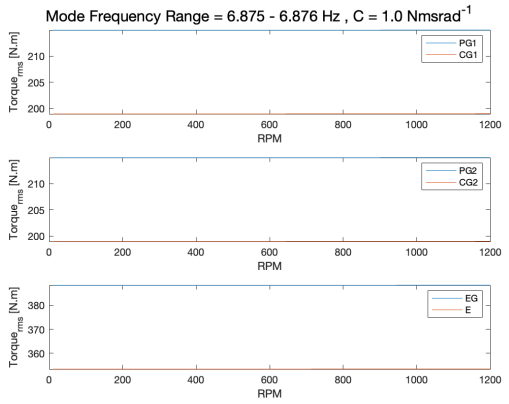

(a) Configuration 1 (Asymmetrical Mode)

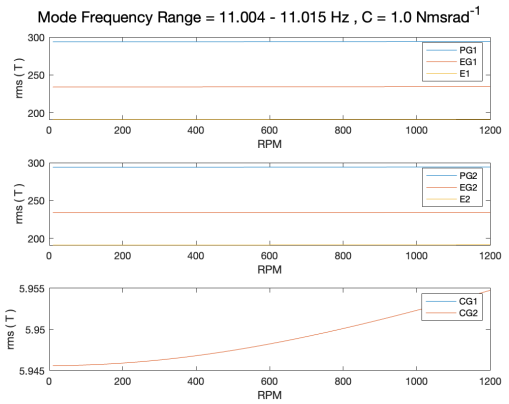

(b) Configuration 2 (Asymmetrical Mode)

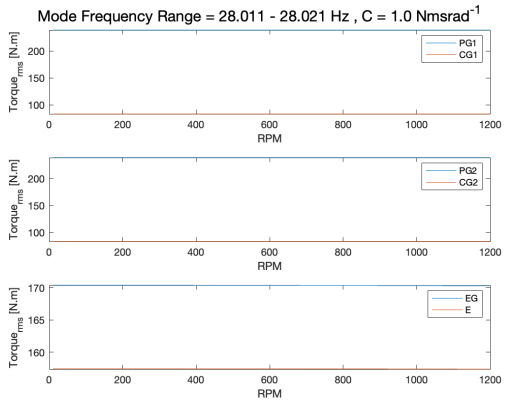

(c) Configuration 1 (Symmetrical Mode)

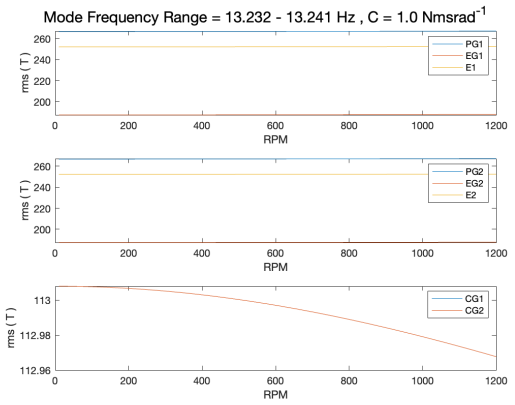

(d) Configuration 2 (Symmetrical Mode)

Figure 49: RMS Torque in Drivetrain Shafts for

6.1. Effect of Dampers

A comparative analysis was performed between symmetric and asymmetric modal responses of the drive-train system under two conditions: (i) uniform blade damping across all blades, and (ii) one blade damper rendered inoperative, thereby introducing an imbalance between Chain 1 and Chain 2.

The results demonstrate the critical importance of asymmetric modes in drive-train dynamic analysis. Under symmetric modal excitation, the inoperative damper condition does not produce significant changes in the global drive-train response. This is expected, as symmetric modes inherently assume identical left-right system behavior, resulting in no differential torque transmission through the interconnect (central gear) shafts.

In contrast, the asymmetric modal response reveals pronounced variations in torque within the central gear shafts when a blade damper is inoperative. The introduced imbalance between the two rotor chains generates differential dynamic loading, which is directly captured by asymmetric modes. These modes therefore provide a more realistic representation of the drive-train behavior under off-nominal or fault conditions.

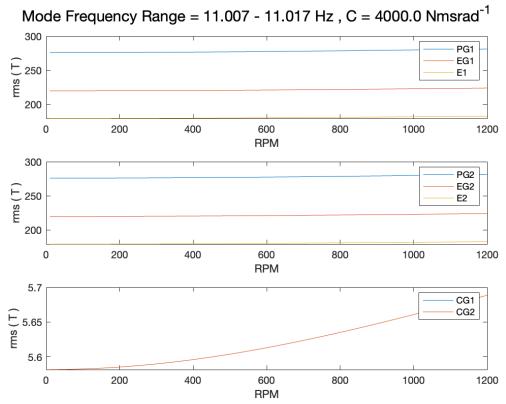

(a) Asymmetrical Mode

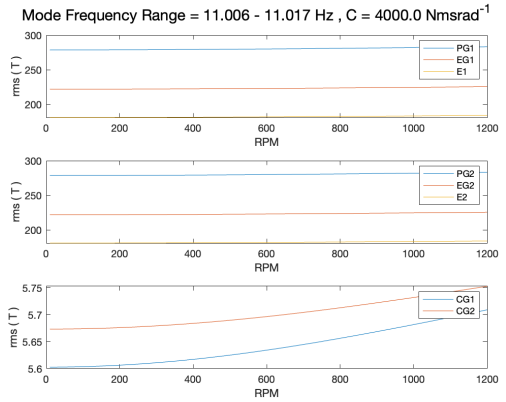

(b) Asymmetrical Mode (One Blade Damper In-Operative)

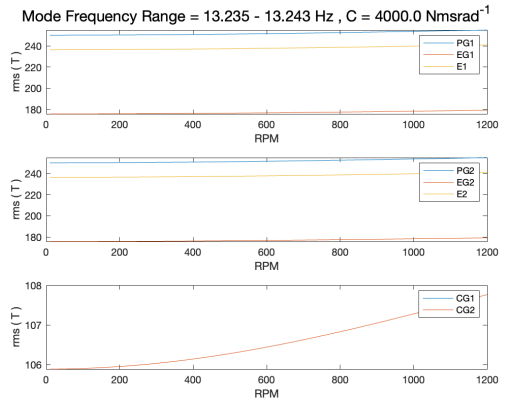

(c) Symmetrical Mode

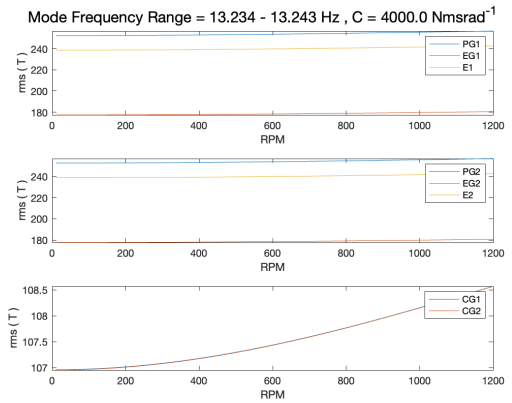

(d) Symmetrical Mode (One Blade Damper In-Operative)

The observed torque perturbations in the interconnect shafts suggest that asymmetric modal analysis is essential for accurately predicting load redistribution and dynamic amplification effects. Furthermore, these perturbations may become more significant when external aerodynamic loads are introduced, potentially leading to additional coupling between structural and aerodynamic excitations.
Comparing Configuration 2 with Configuration 1, the asymmetric modes exhibit negligible changes on the central interconnect shafts for both uniform damping and the one-damper-inoperative cases. Only the torque on the engine gear shaft and engine shaft shows minor variations, attributable to the reduction in damping magnitude.

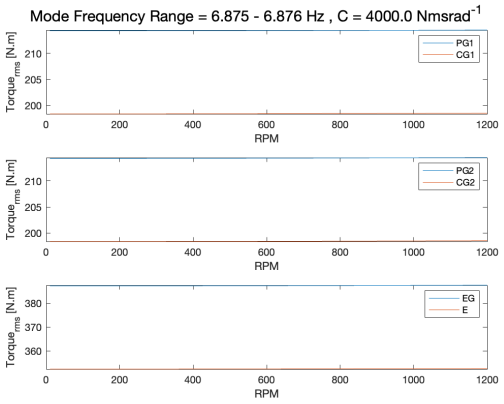

(a) Asymmetrical Mode

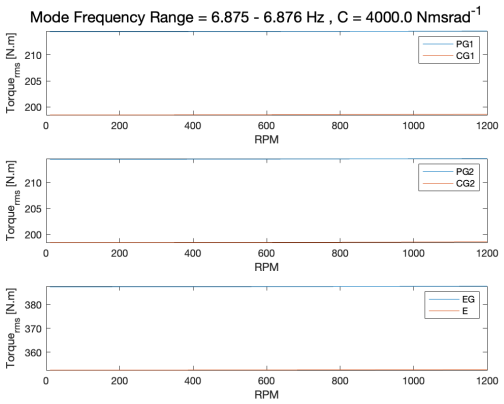

(b) Asymmetrical Mode (One Blade Damper In-Operative)

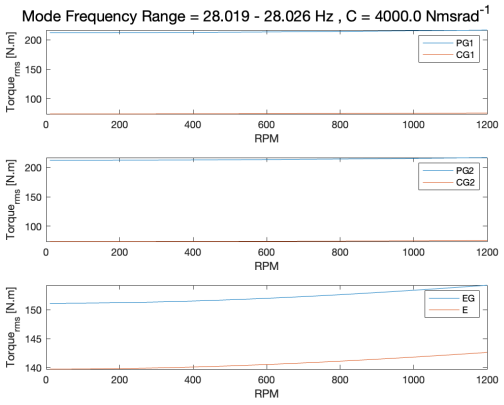

(c) Symmetrical Mode

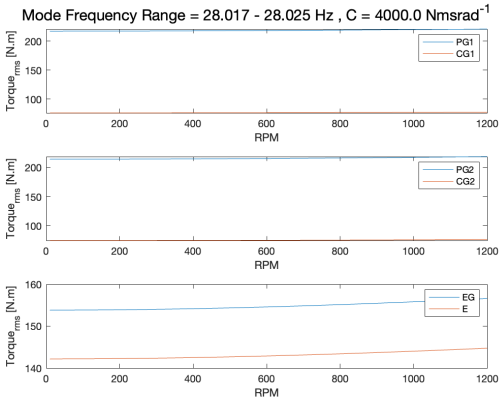

(d) Symmetrical Mode (One Blade Damper In-Operative)

7. Conclusions

This study presents the modeling and analysis of a coupled flexible rotor–drivetrain system for the Tilt rotor configurations. The results demonstrate that the drivetrain is primarily coupled with the rotor collective lead–lag modes. This is evident from the eigenmode shapes obtained for the two configurations, using both the finite element model (FEM) of flexible blades and the transfer matrix method (TMM). The results from these approaches show good agreement with those derived from the mathematical model formulated using multi-blade coordinates (MBC), thereby validating the proposed methodology. Specifically, decomposing the lead–lag response into collective and cyclic components and retaining only the component that directly influences the drivetrain while eliminating the non-coupled components enables effective model order reduction and enhances overall computational efficiency without compromising accuracy. Overall, the study confirms that while symmetric modes are adequate for baseline balanced configurations, asymmetric modes are crucial for evaluating faulted or imbalanced conditions in the drive-train system.

8. Acknowledgements

I would like to express my sincere gratitude to the Prof. Dr. Pierangelo Masarati for their invaluable guidance, constant encouragement, and insightful feedback throughout the course of this research. Their expertise and support were instrumental in shaping the direction and quality of this thesis.

I am also deeply thankful to Bo Li and Catelani Daniele for their technical discussions and support during both challenging and rewarding phases of this work. Their companionship made this journey both manageable and memorable.

Finally, I extend my heartfelt appreciation to my family for their unwavering support, patience, and belief in me. Their sacrifices, understanding, and continuous motivation have been the strongest foundation of my academic pursuit.

References

[1] Accident investigation board report: Cv-22b mishap near yakushima, japan. Technical report, United States Air Force, November 2023. Aircraft T/N 10-0054, 353d Special Operations Wing.

[2] C. W. Jr. Acree. An improved camrad model for aeroelastic stability analysis of the xv-15 with advanced technology blades. Technical report, NASA Ames Research Center, Moffett Field, California.

[3] Bell Helicopter Co. *A Mathematical Model for Real Time Flight Simulation of the Cell Model 301 Tilt Rotor and Research.*

[4] Steven W. Ferguson. A mathematical model for real time flight simulation of a generic tilt-rotor aircraft. NASA Contractor Report CR-166536, National Aeronautics and Space Administration, Ames Research Center, Moffett Field, CA, 1988.

[5] Bo Li, Pierangelo Masarati, and Xiao Wang. Comparative dynamic analysis of tiltrotor drive train configurations using the transfer matrix method. Nanjing, China and Milan, Italy. Nanjing University of Aeronautics and Astronautics and Politecnico di Milano.

[6] Bo Li, Pierangelo Masarati, and Xiao Wang. Parametric eigensolution sensitivity analysis using the transfer matrix method.

[7] Martin Maisel. Tilt rotor research aircraft familiarization document. Technical report, NASA Ames Research Center and U.S. Army Air Mobility R&D Laboratory, Moffett Field, California, January 1975.

[8] Pierangelo Masarati, M. Jihad Ummul Quro, and Andrea Zanoni. Projection continuation for minimal coordinate set formulation and singularity detection of redundantly constrained system dynamics. *Multibody System Dynamics*, 2023.

[9] Aykut Tamer, Pierangelo Masarati, Carlo L. Bottasso, and Luigi Vigevano. Generalized aeroservoelastic stability analysis of rotorcraft. Milan, Italy. Politecnico di Milano.

[10] Xiao Wang and Pinqi Xia. Novel modeling and vibration analysis method on a helicopter drive train system. *AIAA SciTech Forum*, 60, July 2022.